

In the format provided by the authors and unedited.

Coupling N₂ and CO₂ in H₂O to synthesize urea under ambient conditions

Chen Chen^{1,10}, Xiaorong Zhu^{2,10}, Xiaojian Wen^{3,10}, Yangyang Zhou^{1,10}, Ling Zhou¹, Hao Li¹, Li Tao¹, Qiling Li¹, Shiqian Du¹, Tingting Liu¹, Dafeng Yan¹, Chao Xie¹, Yuqin Zou¹, Yanyong Wang¹, Ru Chen¹, Jia Huo¹, Yafei Li^{1,2✉}, Jun Cheng^{1,3✉}, Hui Su⁴, Xu Zhao⁴, Weiren Cheng^{1,4}, Qinghua Liu^{1,4✉}, Hongzhen Lin⁵, Jun Luo^{1,6}, Jun Chen^{1,7✉}, Mingdong Dong^{1,8}, Kai Cheng⁹, Conggang Li^{1,9} and Shuangyin Wang^{1,10✉}

¹State Key Laboratory of Chem/Bio-Sensing and Chemometrics, College of Chemistry and Chemical Engineering, Hunan University, Changsha, P. R. China. ²College of Chemistry and Materials Science, Nanjing Normal University, Nanjing, P. R. China. ³State Key Laboratory of Physical Chemistry of Solid Surfaces, iChEM, College of Chemistry and Chemical Engineering, Xiamen University, Xiamen, P. R. China. ⁴National Synchrotron Radiation Laboratory, University of Science and Technology of China, Hefei, P. R. China. ⁵i-LAB, Suzhou Institute of Nano-Tech and Nano-Bionics, Chinese Academy of Sciences, Suzhou, P. R. China. ⁶Tianjin Key Laboratory of Advanced Functional Porous Materials and Center for Electron Microscopy, School of Materials Science and Engineering, Tianjin University of Technology, Tianjin, P. R. China. ⁷Intelligent Polymer Research Institute, Australian Institute of Innovative Materials, Innovation Campus, University of Wollongong, Wollongong, NSW, Australia. ⁸Interdisciplinary Nanoscience Center, Aarhus University, Aarhus, Denmark. ⁹Key Laboratory of Magnetic Resonance in Biological Systems, State Key Laboratory of Magnetic Resonance and Atomic and Molecular Physics, National Center for Magnetic Resonance in Wuhan Collaborative Innovation Center of Chemistry for Life Sciences, Wuhan Institute of Physics and Mathematics, Chinese Academy of Sciences, Wuhan, P. R. China. ¹⁰These authors contributed equally: Chen Chen, Xiaorong Zhu, Xiaojian Wen, Yangyang Zhou.
✉e-mail: liyafei@njnu.edu.cn; chengjun@xmu.edu.cn; qhliu@ustc.edu.cn; junc@uow.edu.au; shuangyinwang@hnu.edu.cn

Supplementary Information

Coupling N₂ and CO₂ in H₂O to synthesize urea under ambient conditions

Chen Chen^{1†}, Xiaorong Zhu^{2†}, Xiaojian Wen^{3†}, Yangyang Zhou^{1†}, Ling Zhou¹, Hao Li¹, Li Tao¹, Qiling Li¹, Shiqian Du¹, Tingting Liu¹, Dafeng Yan¹, Chao Xie¹, Yuqin Zou¹, Yanyong Wang¹, Ru Chen¹, Jia Huo¹, Yafei Li^{2*}, Jun Cheng^{3*}, Hui Su⁴, Xu Zhao⁴, Weiren Cheng⁴, Qinghua Liu^{4*}, Hongzhen Lin⁵, Jun Luo⁶, Jun Chen^{7*}, Mingdong Dong⁸, Kai Cheng⁹, Conggang Li⁹ and Shuangyin Wang^{1*}

¹State Key Laboratory of Chem/Bio-Sensing and Chemometrics, College of Chemistry and Chemical Engineering, Hunan University, Changsha, Hunan, 410082, P. R. China

²College of Chemistry and Materials Science Nanjing Normal University Nanjing, Jiangsu 210023, P. R. China

³State Key Laboratory of Physical Chemistry of Solid Surfaces, iChEM, College of Chemistry and Chemical Engineering, Xiamen University, Xiamen, 361005, P. R. China

⁴National Synchrotron Radiation Laboratory, University of Science and Technology of China, Hefei, Anhui, 230029, P. R. China

⁵i-LAB, Suzhou Institute of Nano-Tech and Nano-Bionics, Chinese Academy of Sciences, Suzhou 215123, P. R. China

⁶Tianjin Key Laboratory of Advanced Functional Porous Materials and Center for Electron Microscopy, School of Materials Science and Engineering, Tianjin University of Technology, Tianjin 300384, P. R. China

⁷Intelligent Polymer Research Institute, Australian Institute of Innovative Materials, Innovation Campus, University of Wollongong, Northfields Avenue, Wollongong, NSW 2500, Australia

⁸Interdisciplinary Nanoscience Center, Aarhus University, Denmark

⁹Key Laboratory of Magnetic Resonance in Biological Systems, State Key Laboratory of Magnetic Resonance and Atomic and Molecular Physics, National Center for Magnetic Resonance in Wuhan Collaborative Innovation Center of Chemistry for Life Sciences, Wuhan Institute of Physics and Mathematics, Chinese Academy of Sciences, Wuhan 430071, P. R. China

*Correspondence to: shuangyinwang@hnu.edu.cn; liyafei@njnu.edu.cn; chengjun@xmu.edu.cn; qhliu@ustc.edu.cn; junc@uow.edu.au.

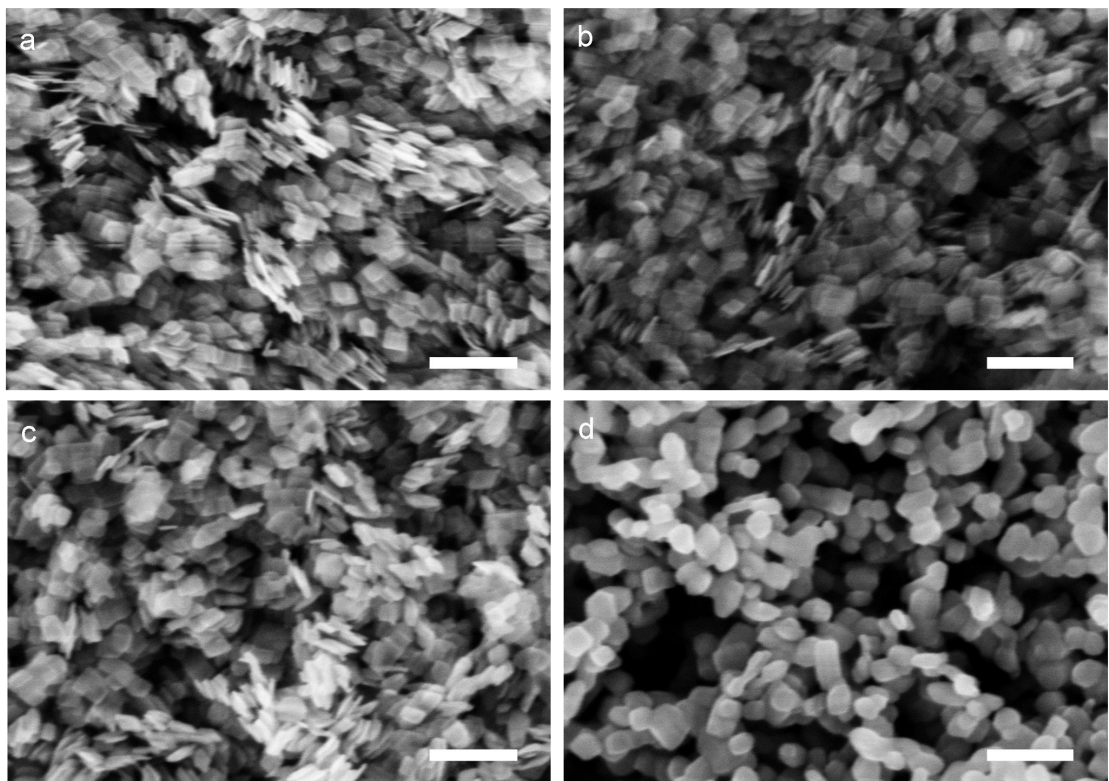
†These authors contributed equally to this work.

Table of contents

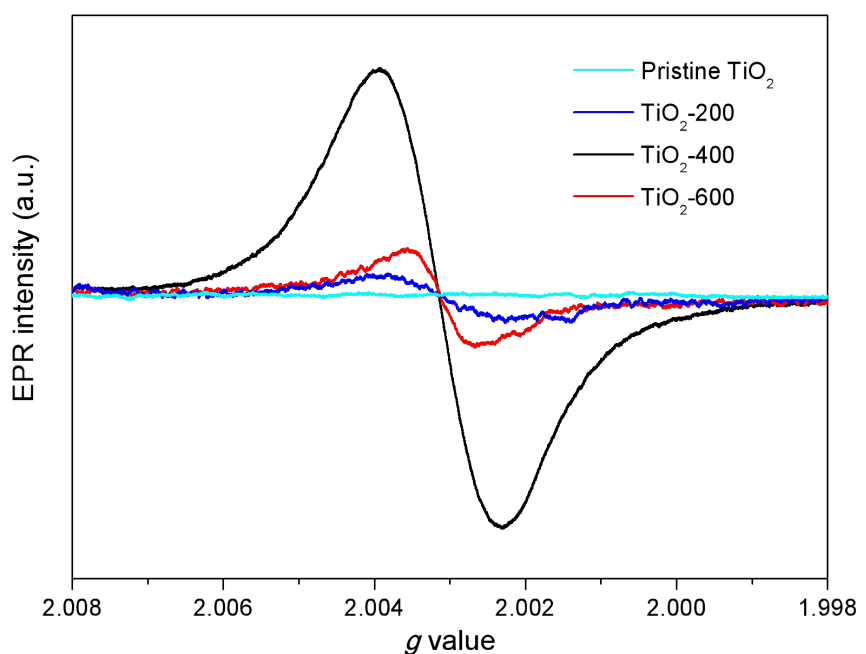
Supplementary Figures 1-43

Supplementary Tables 1-3

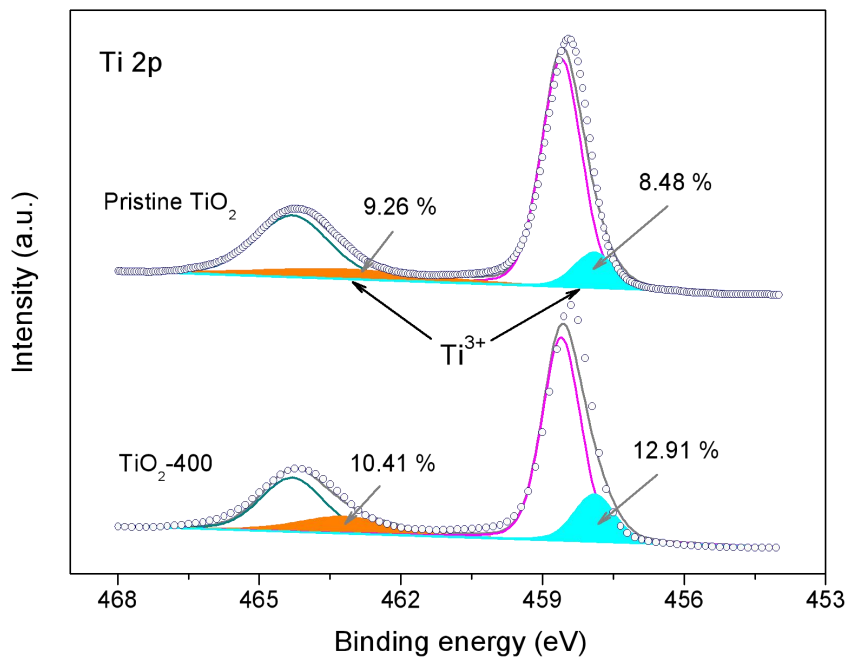
Supplementary References 1-4



Supplementary Figure 1 | SEM images of TiO_2 and $\text{TiO}_2\text{-}X$ (X represents the annealing temperature). (a) TiO_2 . (b) $\text{TiO}_2\text{-}200$. (c) $\text{TiO}_2\text{-}400$ and (d) $\text{TiO}_2\text{-}600$. The inset scale bar is 200 nm.

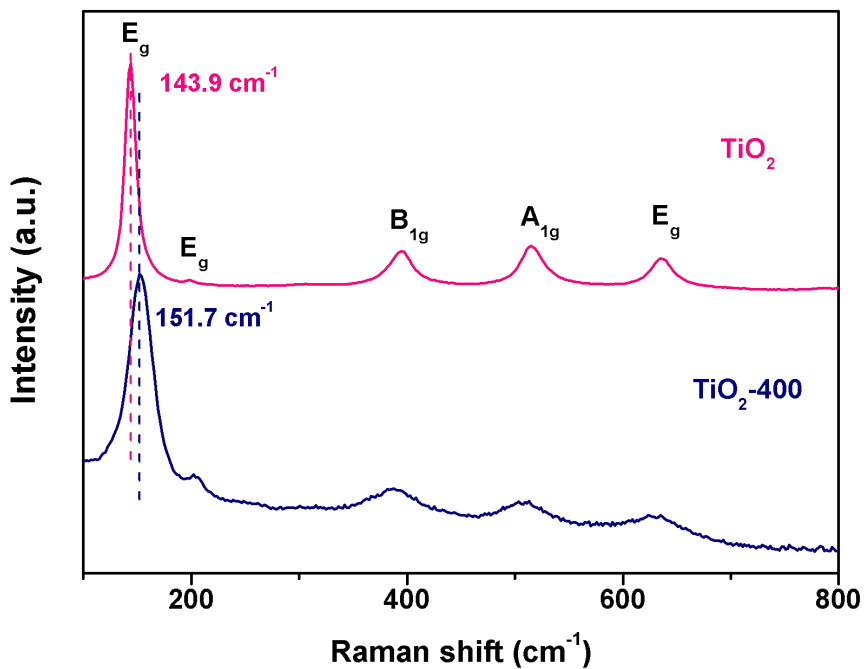


Supplementary Figure 2 | EPR spectra of pristine TiO_2 , TiO_2 -200, TiO_2 -400 and TiO_2 -600.



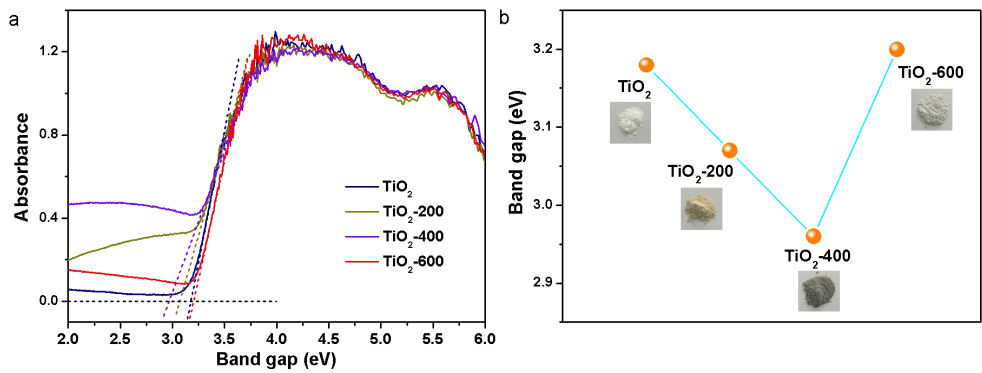
Supplementary Figure 3 | The high-resolution Ti_{2p} XPS spectra of pristine TiO₂ and TiO₂-400.

The high-resolution Ti_{2p} XPS spectra of TiO₂ and TiO₂-400 were obtained to analyze the effect of OV on the electronic structure of TiO₂ (Supplementary Fig. 3). Four peaks centered at 457.9 eV, 458.6 eV, 463.2 eV and 464.3 eV were assigned to Ti³⁺ (2p_{3/2}), Ti⁴⁺ (2p_{3/2}), Ti³⁺ (2p_{1/2}) and Ti⁴⁺ (2p_{1/2}) respectively. Comparing to 8.48 % and 9.46 % for pristine TiO₂, the content of Ti³⁺ (2p_{3/2}) and Ti³⁺ (2p_{1/2}) has increased to 12.91 % and 10.41 % respectively, confirming rich OV in TiO₂-400.



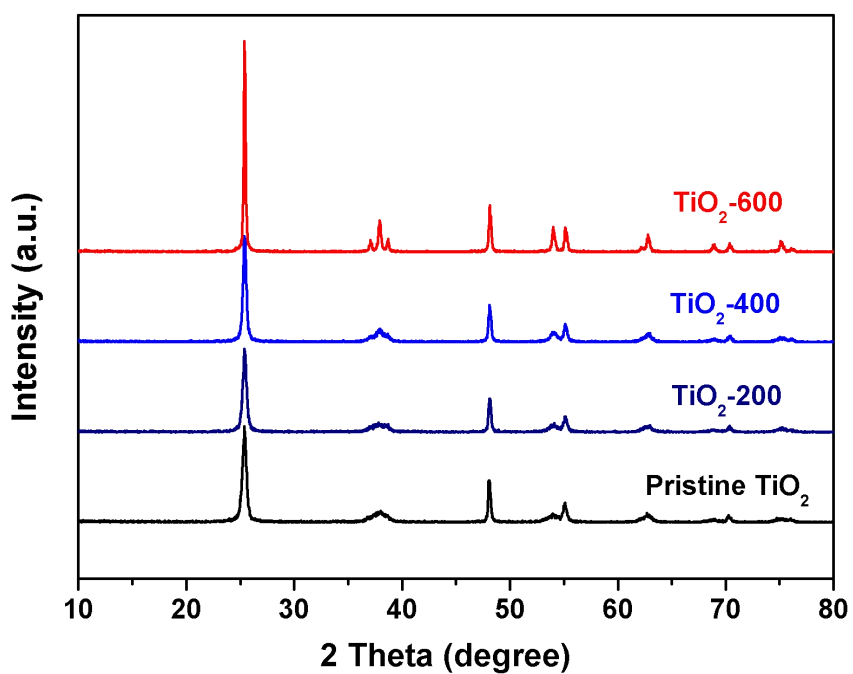
Supplementary Figure 4 | Raman spectra of TiO₂ and TiO₂-400.

As the broadening of main peak (E_g) and shift to higher wavenumber, the existence of oxygen vacancies in TiO₂-400 was confirmed by Raman spectra¹.

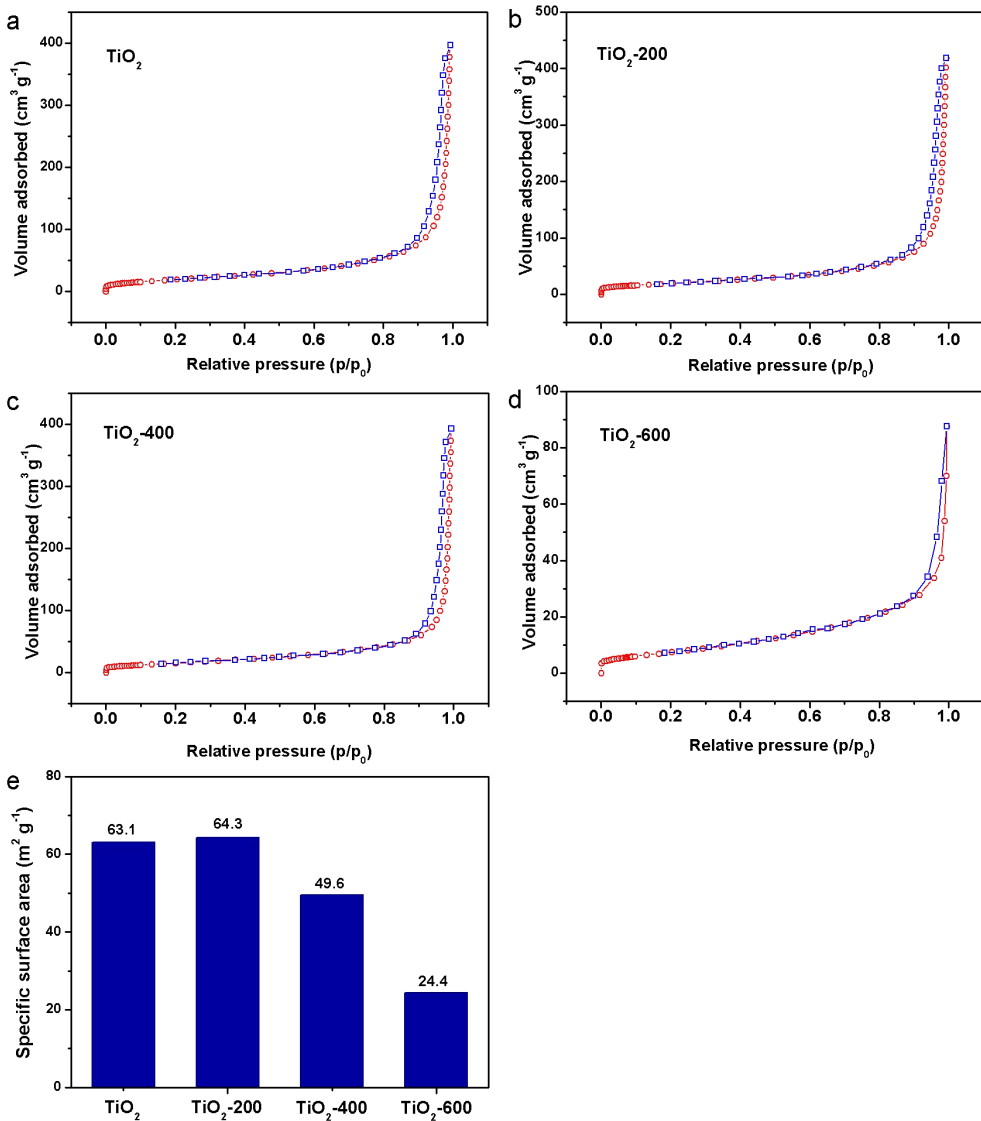


Supplementary Figure 5 | (a) UV-vis diffuse reflectance spectra of TiO_2 , TiO_2 -200, TiO_2 -400 and TiO_2 -600. (b) Band gaps of TiO_2 , TiO_2 -200, TiO_2 -400 and TiO_2 -600, the insets are pictures of the obtained powders.

The band gaps of TiO_2 (3.18 eV), TiO_2 -200 (3.07 eV), TiO_2 -400 (2.96 eV) and TiO_2 -600 (3.20 eV) were acquired and the narrowing band gap of TiO_2 -400 support is associated with the high performance towards urea synthesis.

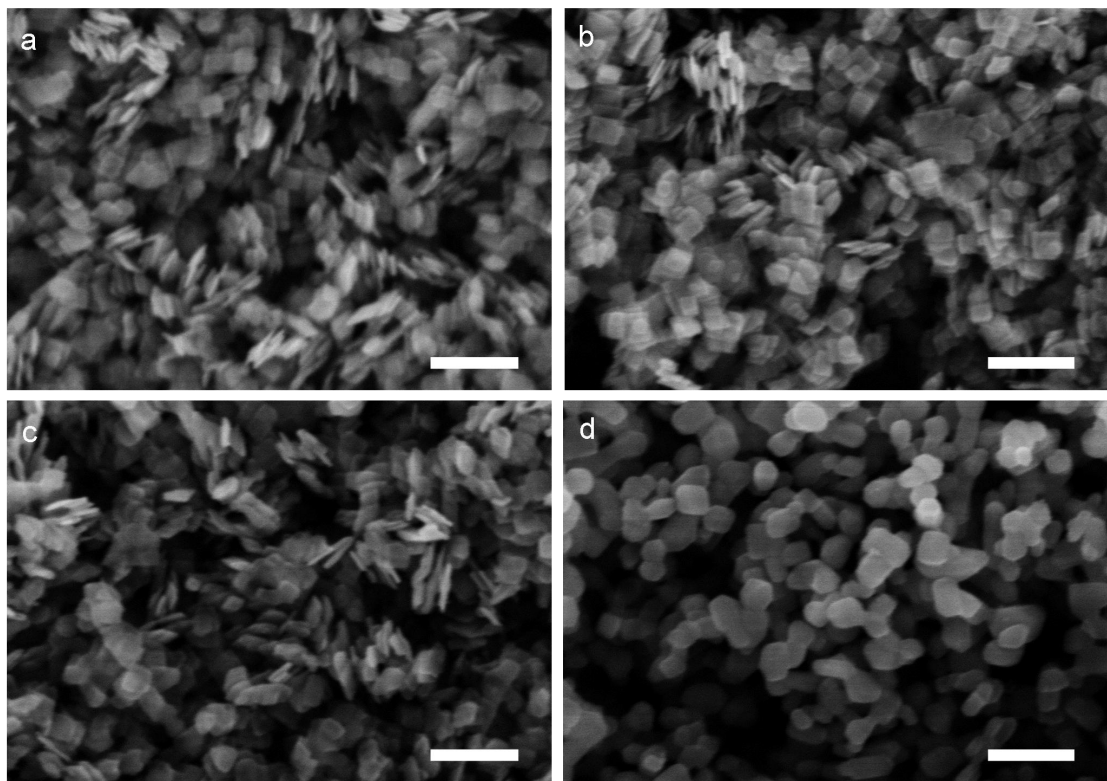


Supplementary Figure 6 | XRD patterns of pristine TiO₂, TiO₂-200, TiO₂-400 and TiO₂-600.
The XRD patterns of pristine TiO₂ and TiO₂ with treatment show typical anatase feature. From the results we can obtained that the grain size and crystalline of TiO₂-600 was obvious enlarged, corresponding to the results of SEM.

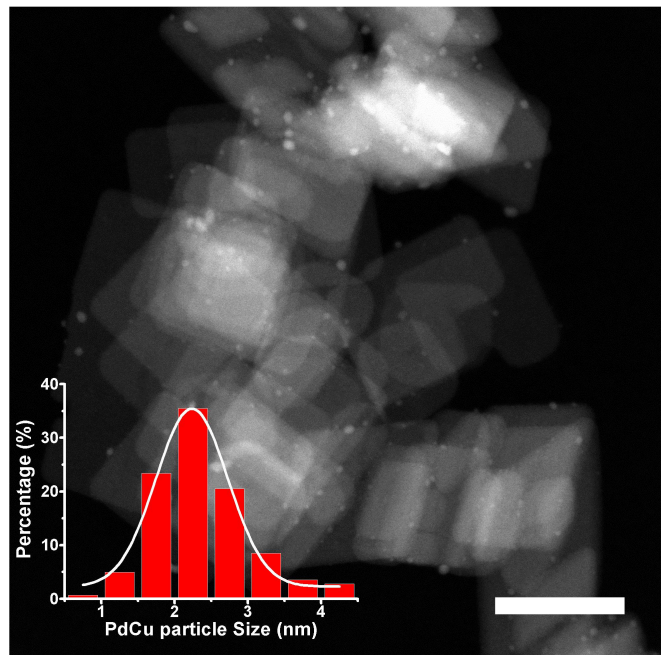


Supplementary Figure 7 | (a) The N₂ adsorption-desorption isotherms of TiO₂. (b) The N₂ adsorption-desorption isotherms of TiO₂-200. (c) The N₂ adsorption-desorption isotherms of TiO₂-400. (d) The N₂ adsorption-desorption isotherms of TiO₂-600. (e) The specific surface areas of TiO₂, TiO₂-200, TiO₂-400 and TiO₂-600.

As presented in Supplementary Fig. 7, the Brunauer-Emmett-Teller (BET) specific surface areas of TiO₂ (63.1 m² g⁻¹), TiO₂-200 (64.3 m² g⁻¹), TiO₂-400 (49.6 m² g⁻¹) and TiO₂-600 (24.4 m² g⁻¹) are obtained and the sharply decreased value of TiO₂-600 also confirms the aggregation of TiO₂ nanosheets.

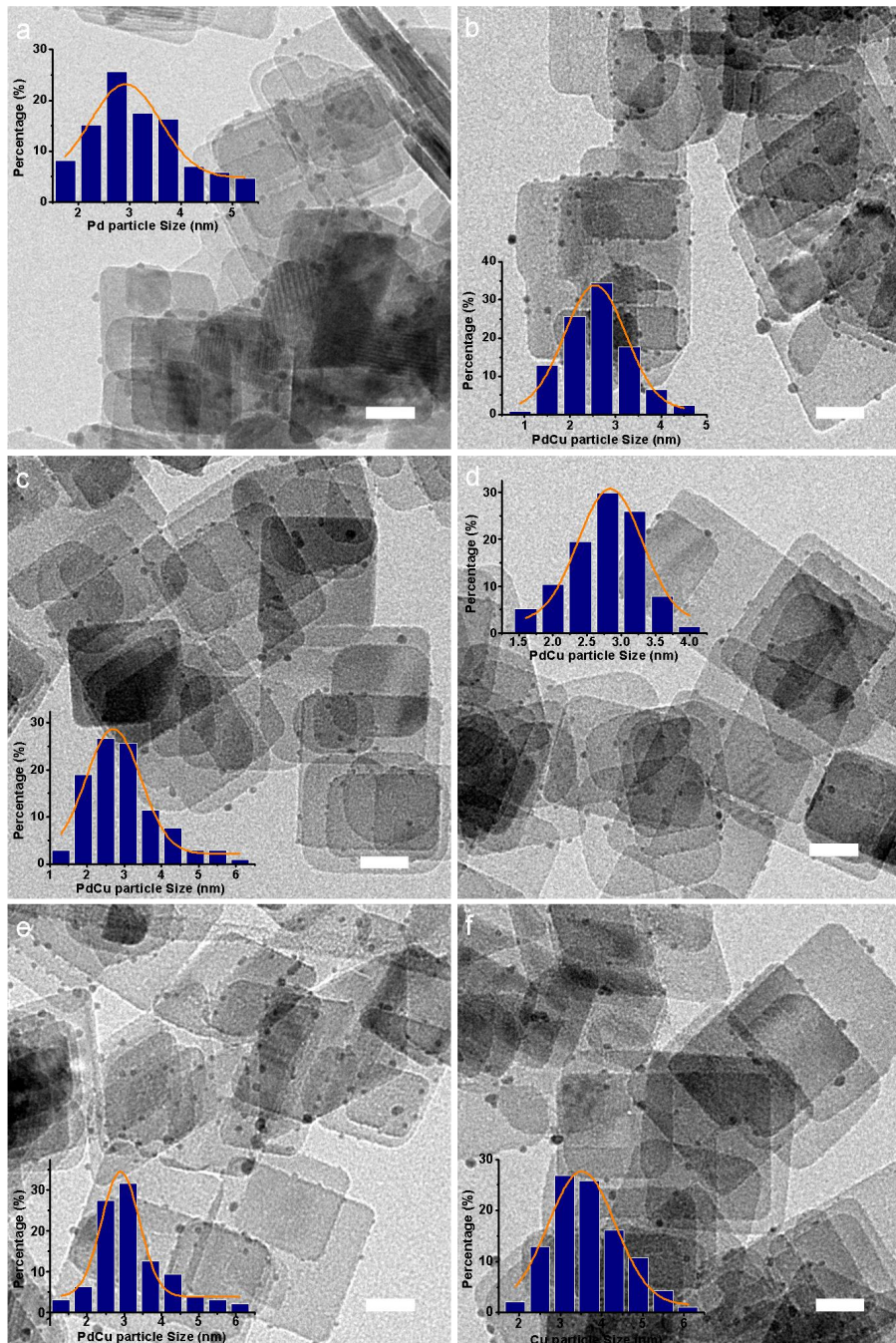


Supplementary Figure 8 | SEM images of $\text{Pd}_1\text{Cu}_1/\text{TiO}_2$ and $\text{Pd}_1\text{Cu}_1/\text{TiO}_2\text{-}X$ (X represents the annealing temperature). (a) $\text{Pd}_1\text{Cu}_1/\text{TiO}_2$. (b) $\text{Pd}_1\text{Cu}_1/\text{TiO}_2\text{-}200$. (c) $\text{Pd}_1\text{Cu}_1/\text{TiO}_2\text{-}400$ and (d) $\text{Pd}_1\text{Cu}_1/\text{TiO}_2\text{-}600$. The inset scale bar is 200 nm.



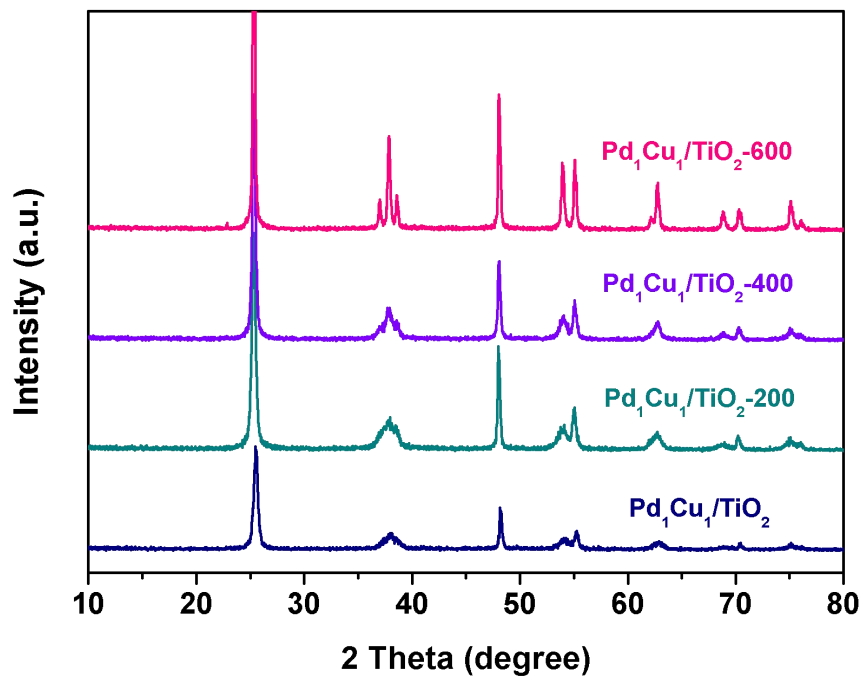
Supplementary Figure 9 | TEM images of the $\text{Pd}_1\text{Cu}_1/\text{TiO}_2$ and the corresponding distribution of particle size. The inset scale bar is 50 nm.

As illustrated in Supplementary Fig. 9, transmission electron microscopy (TEM) image exhibits the nanosheet structure of $\text{Pd}_1\text{Cu}_1/\text{TiO}_2$ and the nanoparticles with uniform size distribution (2-3 nm) are distributed homogeneously on the TiO_2 nanosheet.



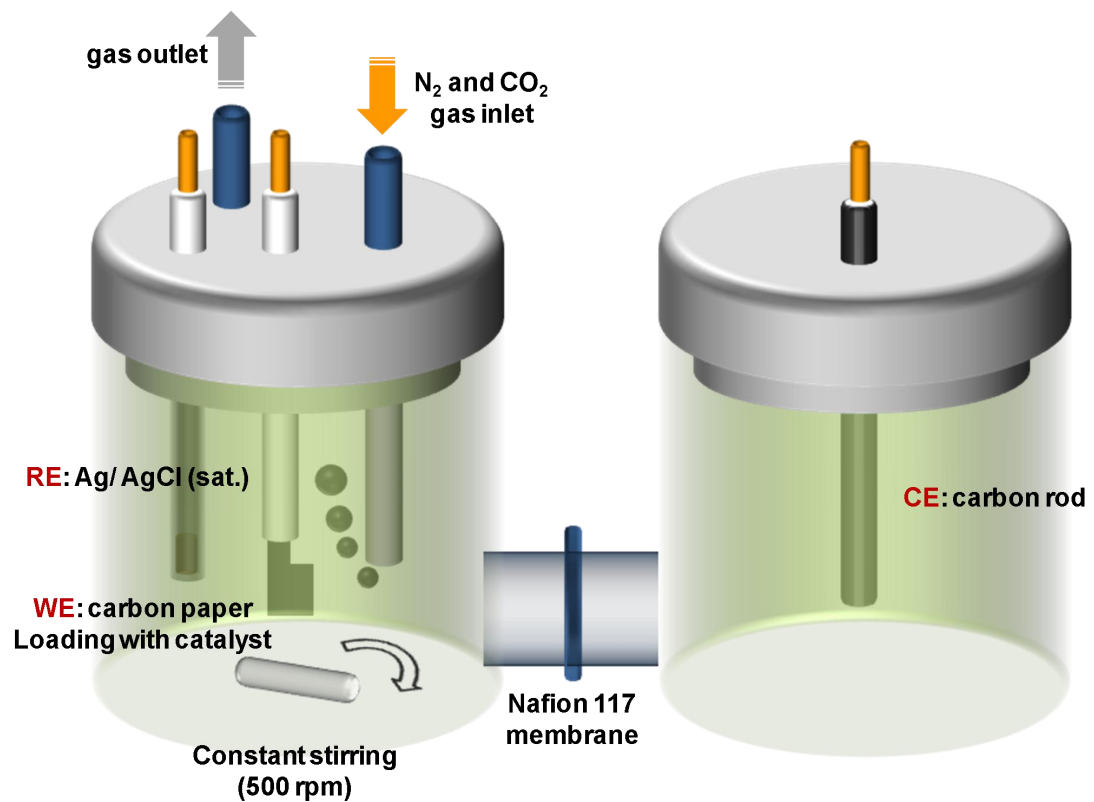
Supplementary Figure 10 | TEM images of the electrocatalysts and the corresponding distribution of particle size. (a) Pd/TiO₂. (b) Pd₃Cu₁/TiO₂. (c) Pd₂Cu₁/TiO₂. (d) Pd₁Cu₂/TiO₂. (e) Pd₁Cu₃/TiO₂. and (f) Cu/TiO₂. The inset scale bar is 20 nm.

Transmission electron microscopy (TEM) images in Supplementary Fig. 10 exhibit the maintaining of nanosheet structure for electrocatalysts with metal loadings. The nanoparticles with uniform size distribution are distributed homogeneously on the TiO₂ nanosheet for each catalyst.

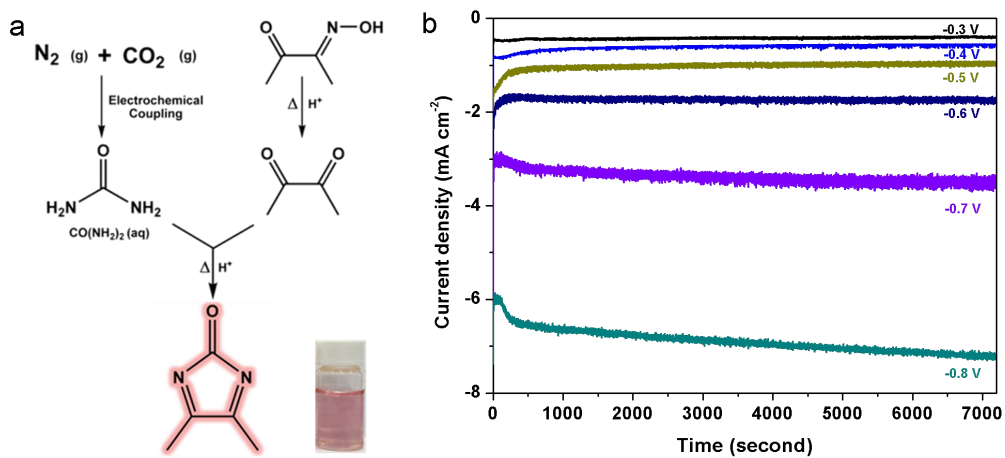


Supplementary Figure 11 | XRD patterns of Pd/TiO₂, Pd₃Cu₁/TiO₂, Pd₂Cu₁/TiO₂, Pd₁Cu₁/TiO₂, Pd₁Cu₂/TiO₂, Pd₁Cu₃/TiO₂ and Cu/TiO₂.

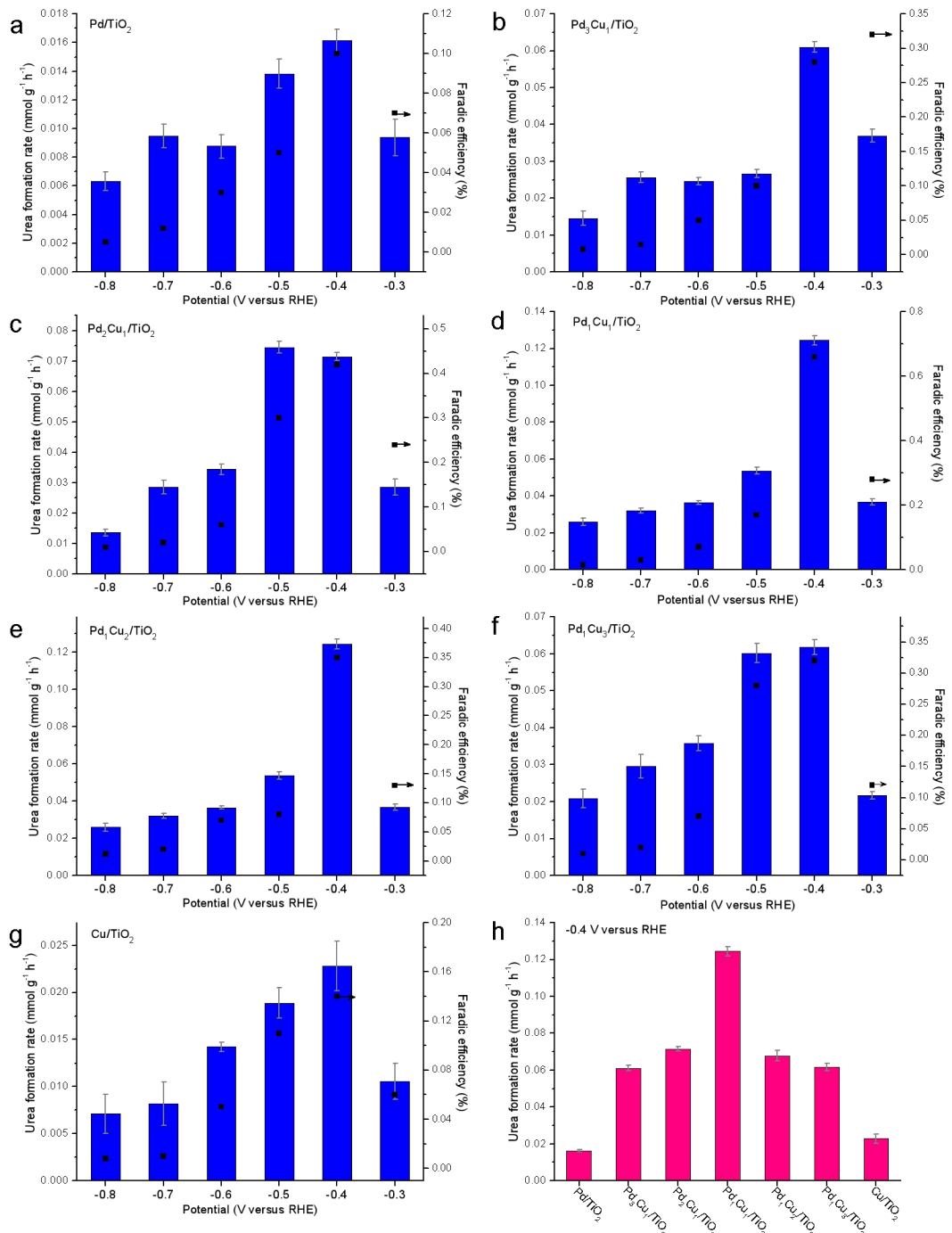
The X-ray diffraction (XRD) patterns of electrocatalysts show the maintaining of the character peaks for anatase TiO₂, but there is no obvious peak for Pd and Cu attributing to the highly crystalline of TiO₂ and low loading of nanoparticles.



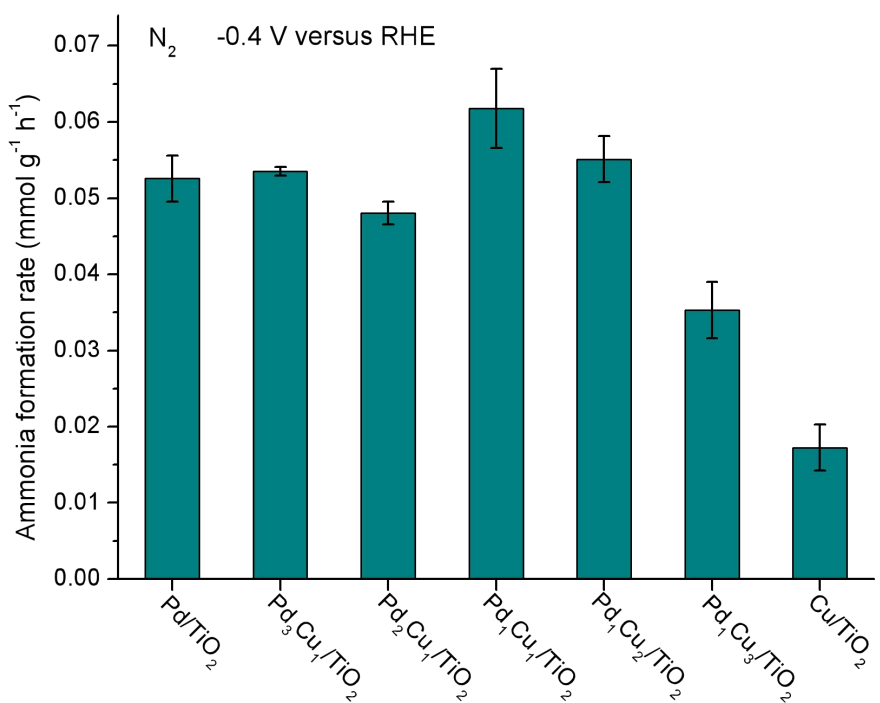
Supplementary Figure 12 | Schematic diagram of the H-type cell (H-cell) for urea synthesis.



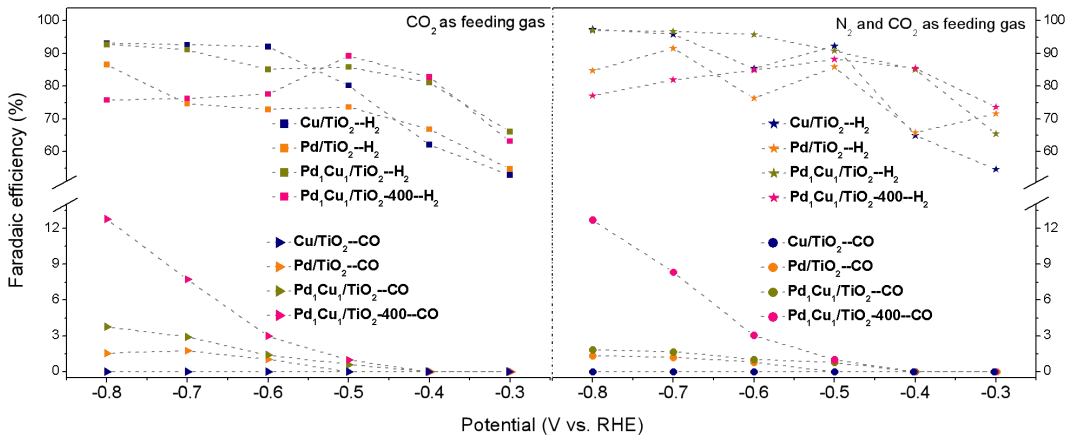
Supplementary Figure 13 | (a) Experimental scheme for the electrochemical synthesis of urea and subsequent determination of the urea concentration generated. Urea detection is based on the diacetyl monoxime method and the inset is the picture of acquired pink solution. (b) Chronoamperometric curves of $\text{Pd}_1\text{Cu}_1/\text{TiO}_2$ at different applied potentials in H cell.



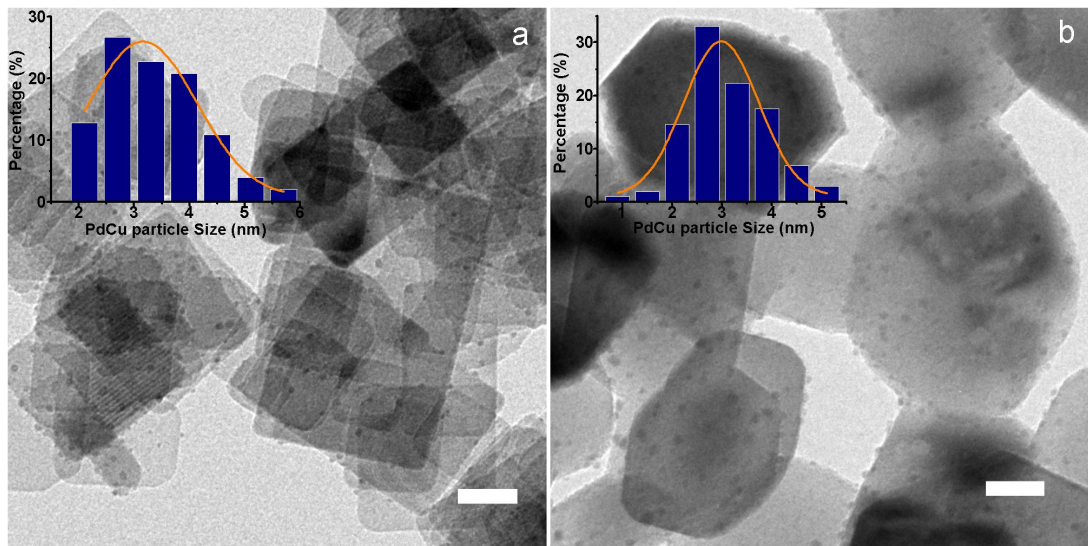
Supplementary Figure 14 | Evaluation of urea formation rates in H cell for electrocatalysts. Urea formation rates and corresponding Faradic efficiencies of (a) Pd/TiO_2 , (b) $\text{Pd}_3\text{Cu}_1/\text{TiO}_2$, (c) $\text{Pd}_2\text{Cu}_1/\text{TiO}_2$, (d) $\text{Pd}_1\text{Cu}_1/\text{TiO}_2$, (e) $\text{Pd}_1\text{Cu}_2/\text{TiO}_2$, (f) $\text{Pd}_1\text{Cu}_3/\text{TiO}_2$ and (g) Cu/TiO_2 at various potentials. (h) Urea formation rates and corresponding Faradic efficiencies for various electrocatalysts at -0.4 V versus RHE.



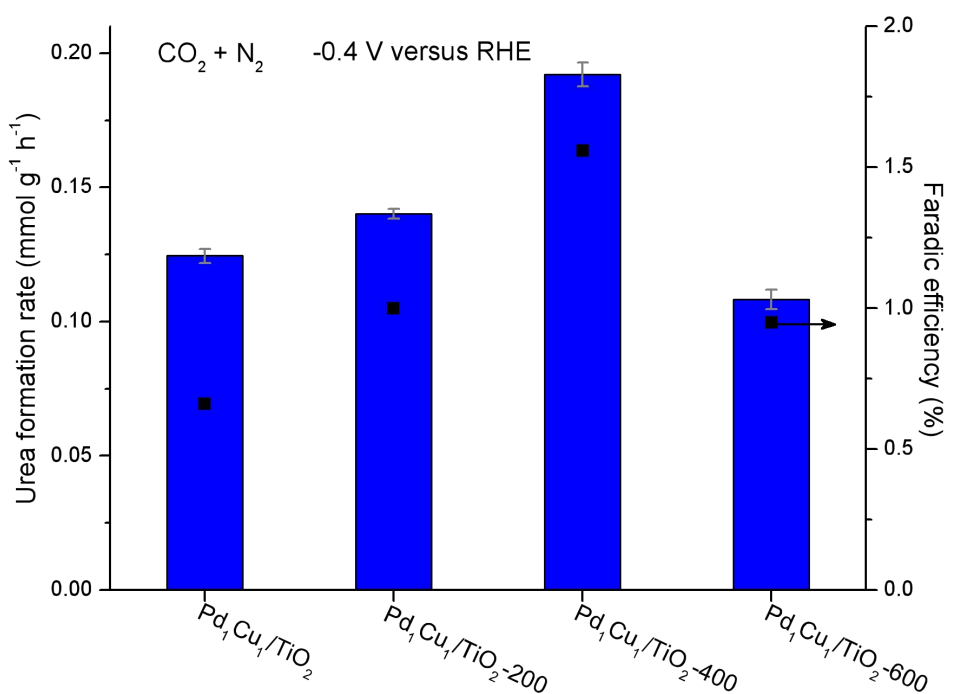
Supplementary Figure 15 | Evaluation of ammonia formation rates in H cell for electrocatalysts at -0.4 V versus RHE.



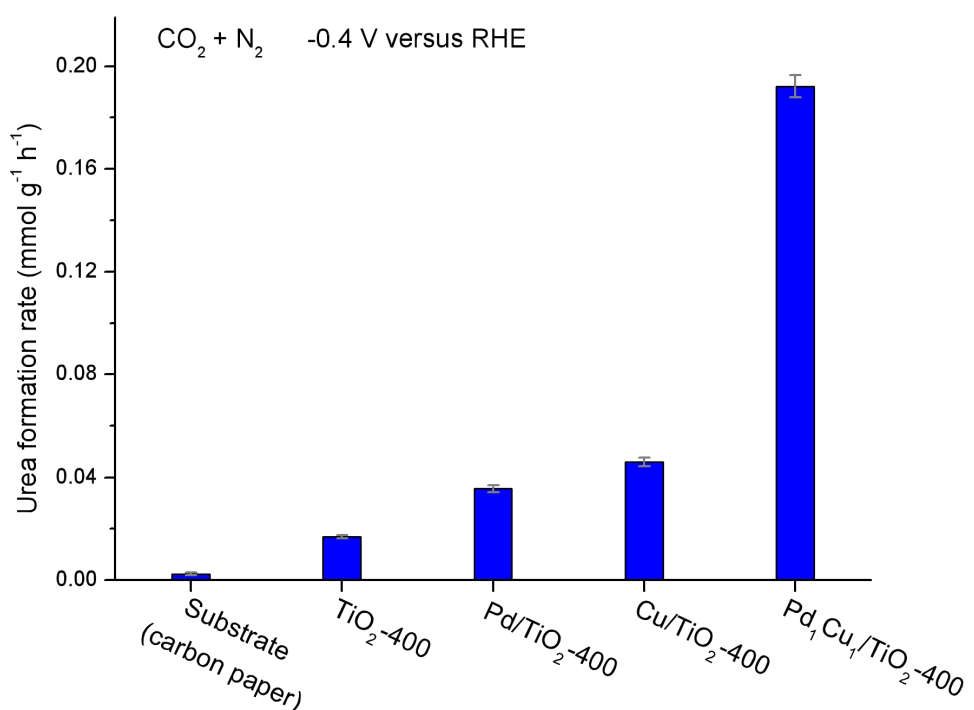
Supplementary Figure 16 | Electrochemical CO_2 reduction performances of Cu/TiO_2 , Pd/TiO_2 , $\text{Pd}_1\text{Cu}_1/\text{TiO}_2$ and $\text{Pd}_1\text{Cu}_1/\text{TiO}_2\text{-}400$ with CO_2 or the mixing of N_2 and CO_2 as feeding gas in H cell.



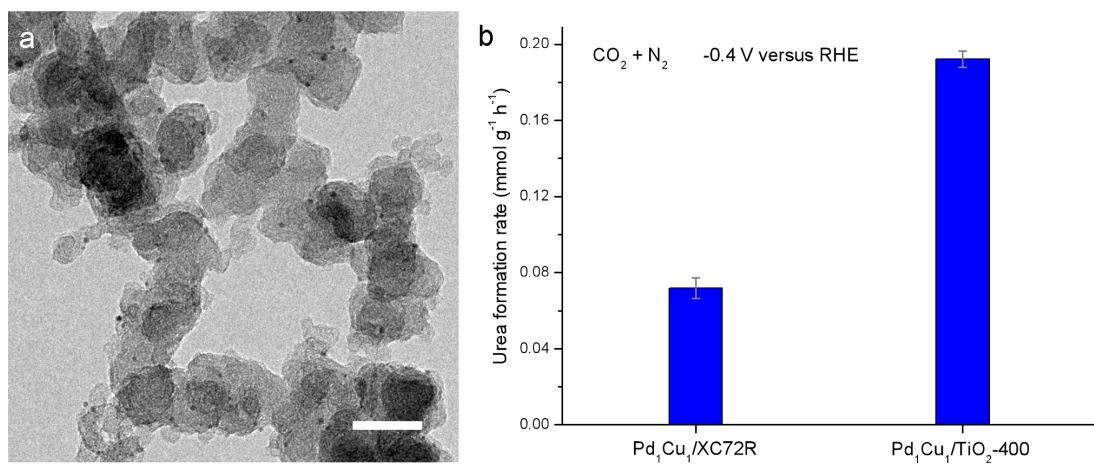
Supplementary Figure 17 | TEM images of the (a) Pd₁Cu₁/TiO₂-200 and (b) Pd₁Cu₁/TiO₂-600. The inset pictures display the corresponding distributions of particle size and the inset scale bar is 20 nm.



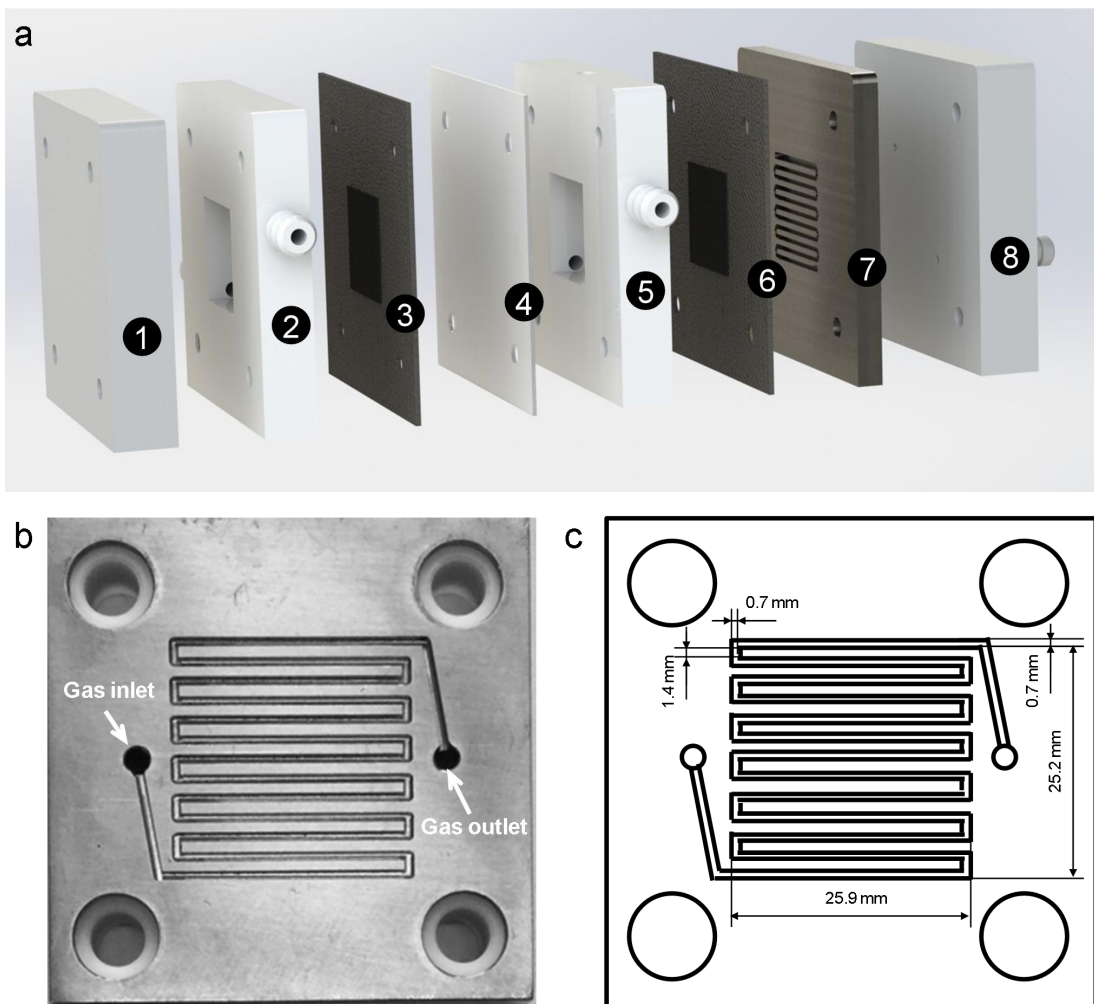
Supplementary Figure 18 | The urea formation rates of Pd₁Cu₁/TiO₂, Pd₁Cu₁/TiO₂-200, Pd₁Cu₁/TiO₂-400 and Pd₁Cu₁/TiO₂-600 at -0.4 V versus RHE in H cell.



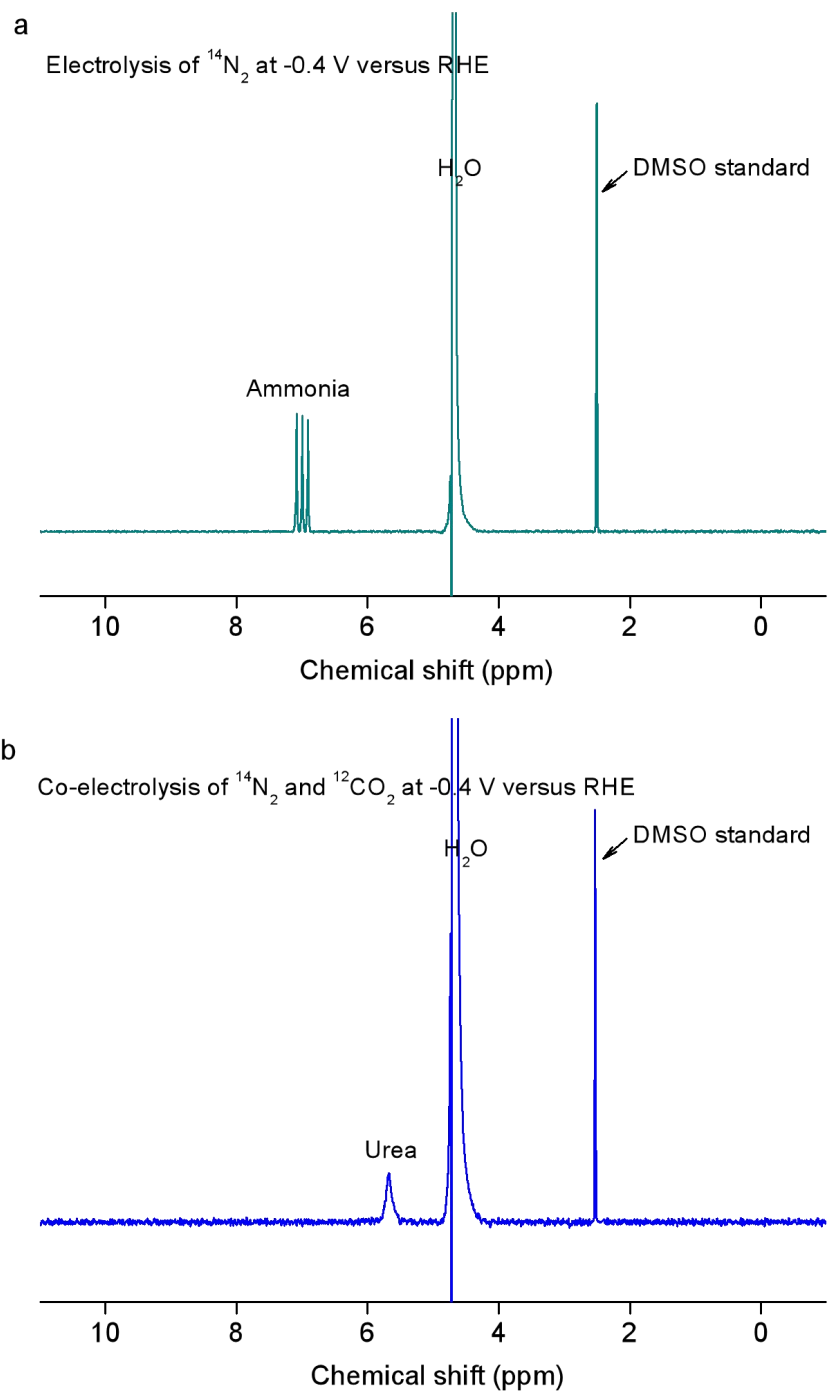
Supplementary Figure 19 | The urea formation rates of carbon paper, $\text{TiO}_2\text{-}400$, $\text{Pd}/\text{TiO}_2\text{-}400$, $\text{Cu}/\text{TiO}_2\text{-}400$ and $\text{Pd}_1\text{Cu}_1/\text{TiO}_2\text{-}400$ at -0.4 V versus RHE in H cell.



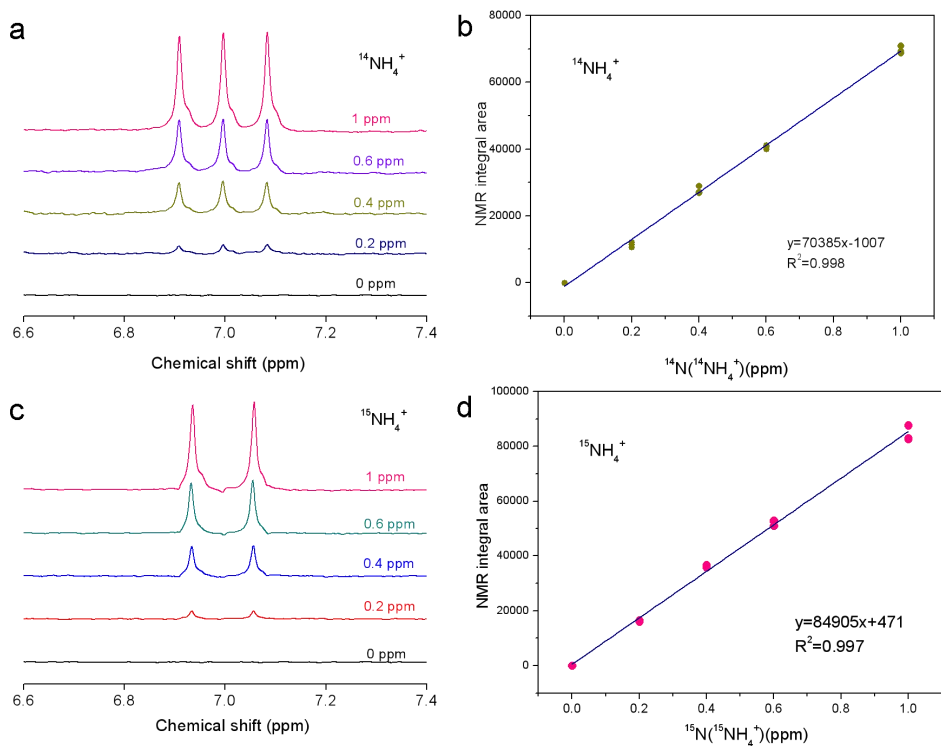
Supplementary Figure 20 | (a) The TEM image of $\text{Pd}_1\text{Cu}_1/\text{XC72R}$. (b) The urea formation rates of $\text{Pd}_1\text{Cu}_1/\text{XC72R}$ and $\text{Pd}_1\text{Cu}_1/\text{TiO}_2\text{-400}$ at -0.4 V versus RHE in H cell. The inset scale bar is 50 nm.



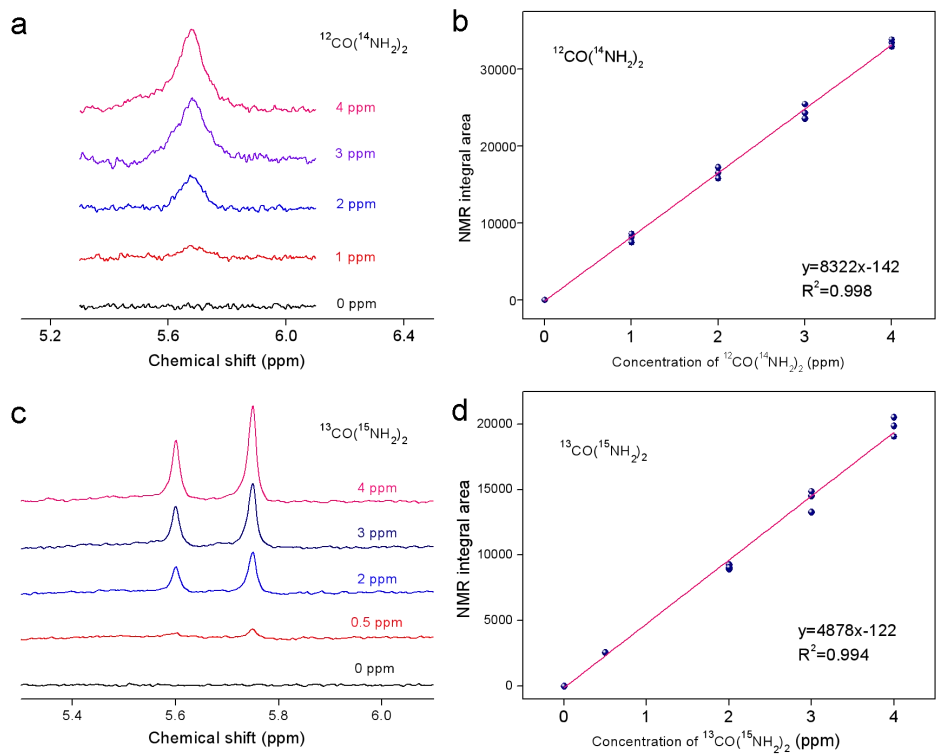
Supplementary Figure 21 | (a) Design of flow cell. ①, ②, ⑤ and ⑧: Electrode holder. ③: Anode. ④: Anion exchange membrane. ⑥ Cathode. ⑦: Titanium flowplate. (b) The real photo of titanium flowplate. (c) The specific size of flow field.



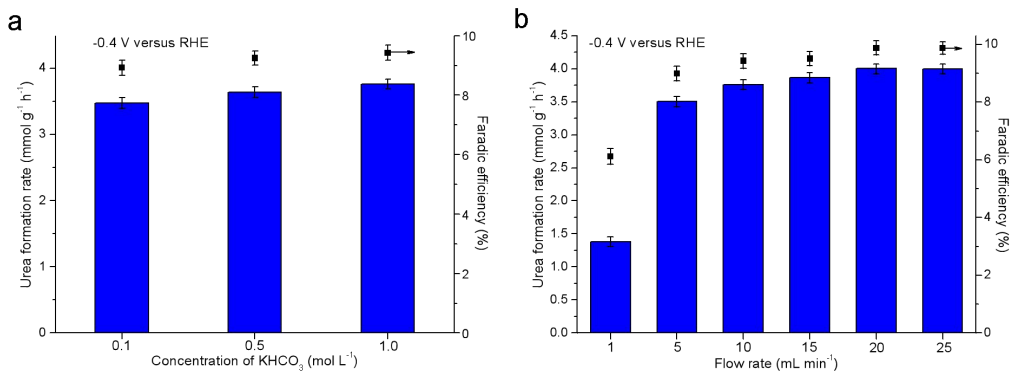
Supplementary Figure 22 | The full representative NMR spectra for (a) electrochemical N_2 reduction and (b) co-electrolysis of N_2 and CO_2 .



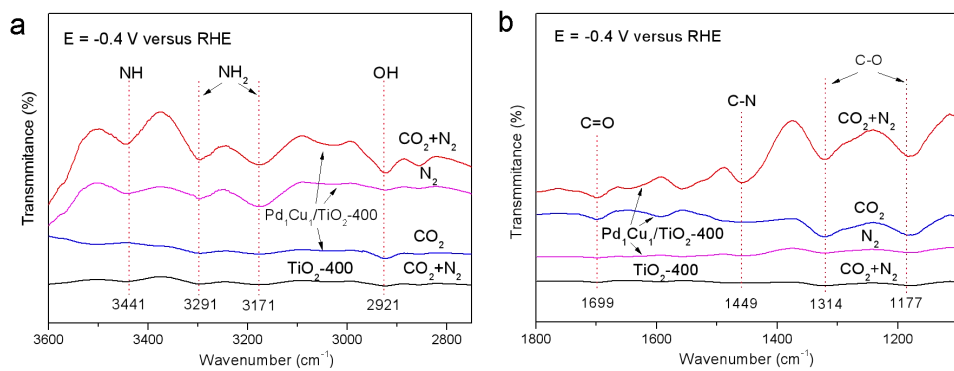
Supplementary Figure 23 | NMR spectra and calibration curves for quantification of ammonia. (a) NMR spectra of $^{14}\text{NH}_4^+$ with various concentrations. (b) The calibration curves for $^{14}\text{NH}_4^+$. (c) NMR spectra of $^{15}\text{NH}_4^+$ with various concentrations. (d) The calibration curves for $^{15}\text{NH}_4^+$.



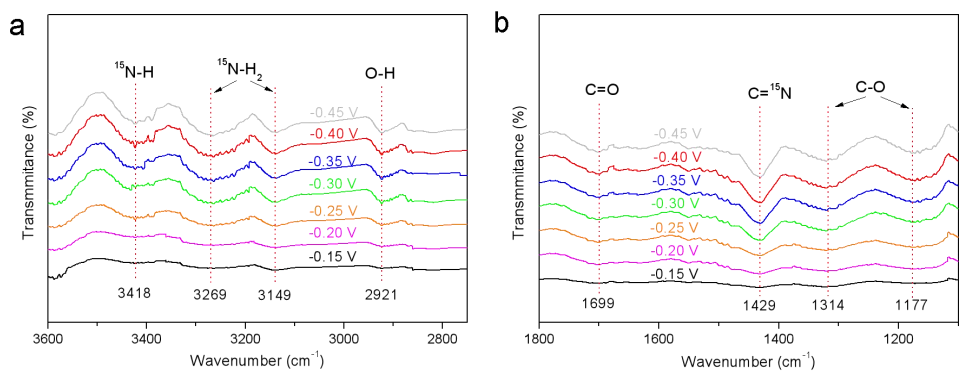
Supplementary Figure 24 | NMR spectra and calibration curves for quantification of urea. (a) NMR spectra of $^{12}\text{CO}(^{14}\text{NH}_2)_2$ with various concentrations. (b) The calibration curves for $^{12}\text{CO}(^{14}\text{NH}_2)_2$. (c) NMR spectra of $^{13}\text{CO}(^{15}\text{NH}_2)_2$ with various concentrations. (d) The calibration curves for $^{13}\text{CO}(^{15}\text{NH}_2)_2$.



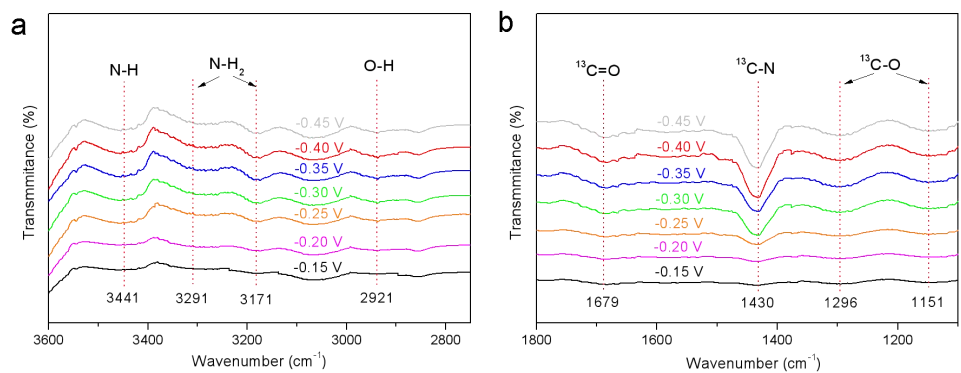
Supplementary Figure 25 | (a) The urea formation rates and the corresponding Faradic efficiencies of $\text{Pd}_1\text{Cu}_1/\text{TiO}_2$ -400 at -0.4 V versus RHE in various concentrations of electrolytes, the electrolyte flow rate is 10 mL min^{-1} . (b) The urea formation rates and the corresponding Faradic efficiencies of $\text{Pd}_1\text{Cu}_1/\text{TiO}_2$ -400 at -0.4 V versus RHE with various electrolyte flow rates in 1.0 M KHCO_3 .



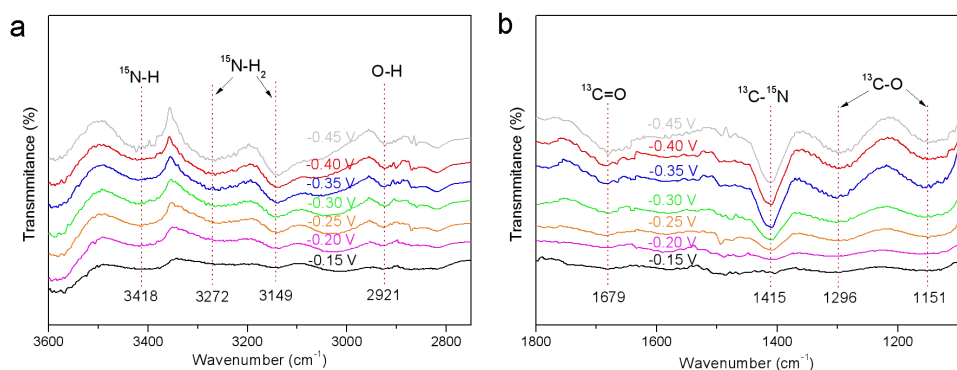
Supplementary Figure 26 | IR signals in the range 2750-3600 cm^{-1} (a) and in the range 1100-1800 cm^{-1} (b) under -0.4 V versus RHE for Pd₁Cu₁/TiO₂-400 during the electroreduction of N₂ or CO₂ processes and for TiO₂-400 during the electroreduction of N₂ and CO₂ processes.



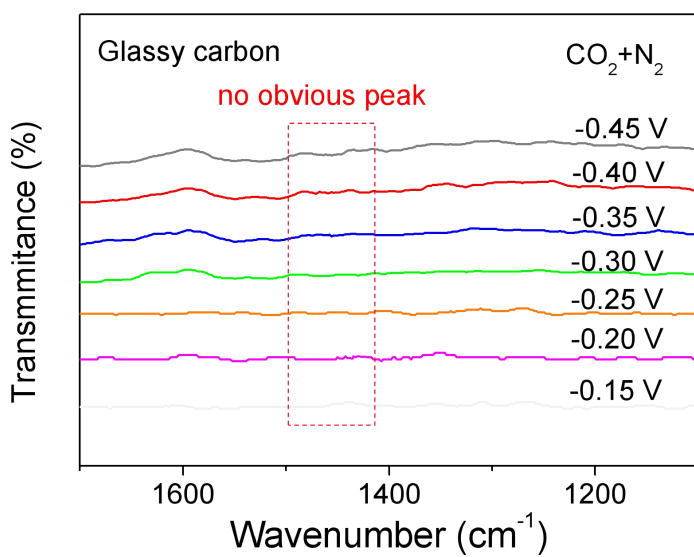
Supplementary Figure 27 | IR signals in the range 2750-3600 cm⁻¹ (a) and in the range 1100-1800 cm⁻¹ (b) under various potentials for Pd₁Cu₁/TiO₂-400 during the electroreduction of ¹⁵N₂ and ¹²CO₂ processes.



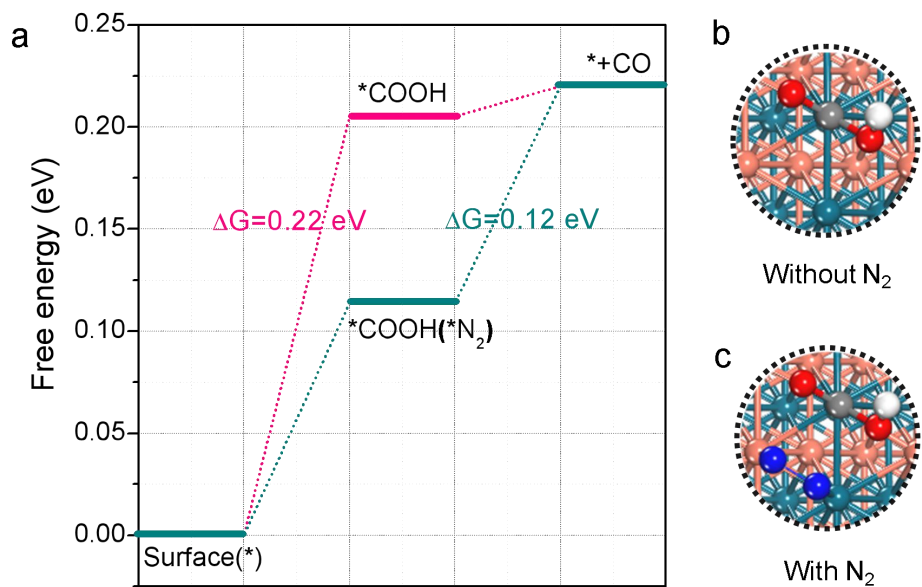
Supplementary Figure 28 | IR signals in the range 2750-3600 cm^{-1} (a) and in the range 1100-1800 cm^{-1} (b) under various potentials for $\text{Pd}_1\text{Cu}_1/\text{TiO}_2$ -400 during the electroreduction of $^{14}\text{N}_2$ and $^{13}\text{CO}_2$ processes.



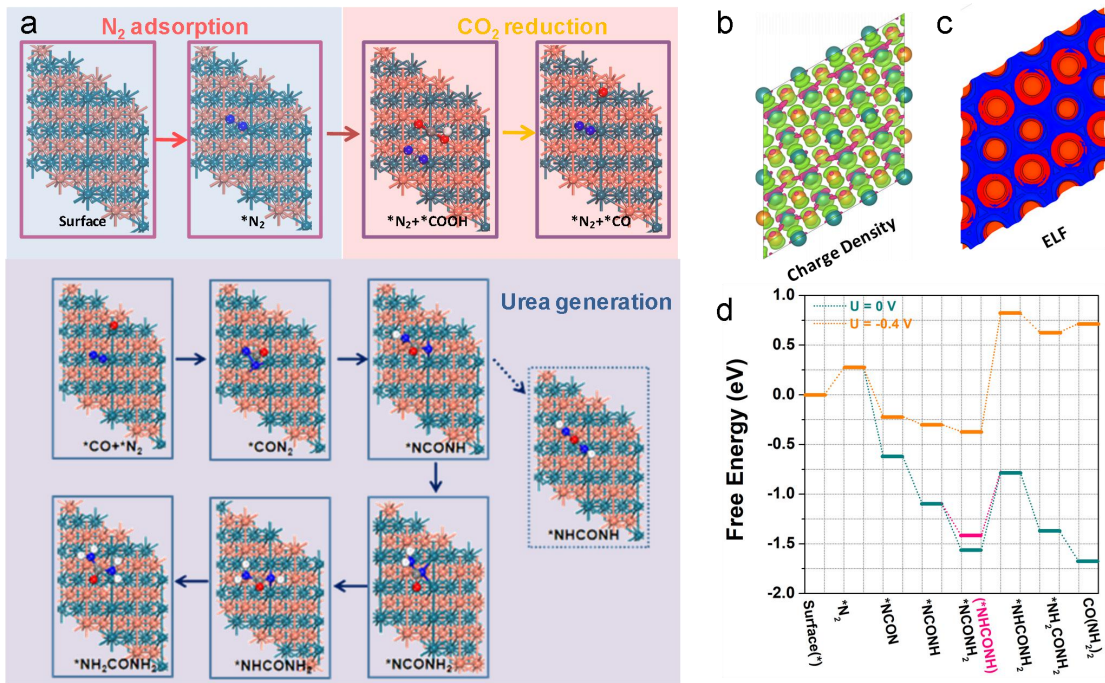
Supplementary Figure 29 | IR signals in the range 2750-3600 cm^{-1} (a) and in the range 1100-1800 cm^{-1} (b) under various potentials for $\text{Pd}_1\text{Cu}_1/\text{TiO}_2$ -400 during the electrocoupling of $^{15}\text{N}_2$ and $^{13}\text{CO}_2$ processes.



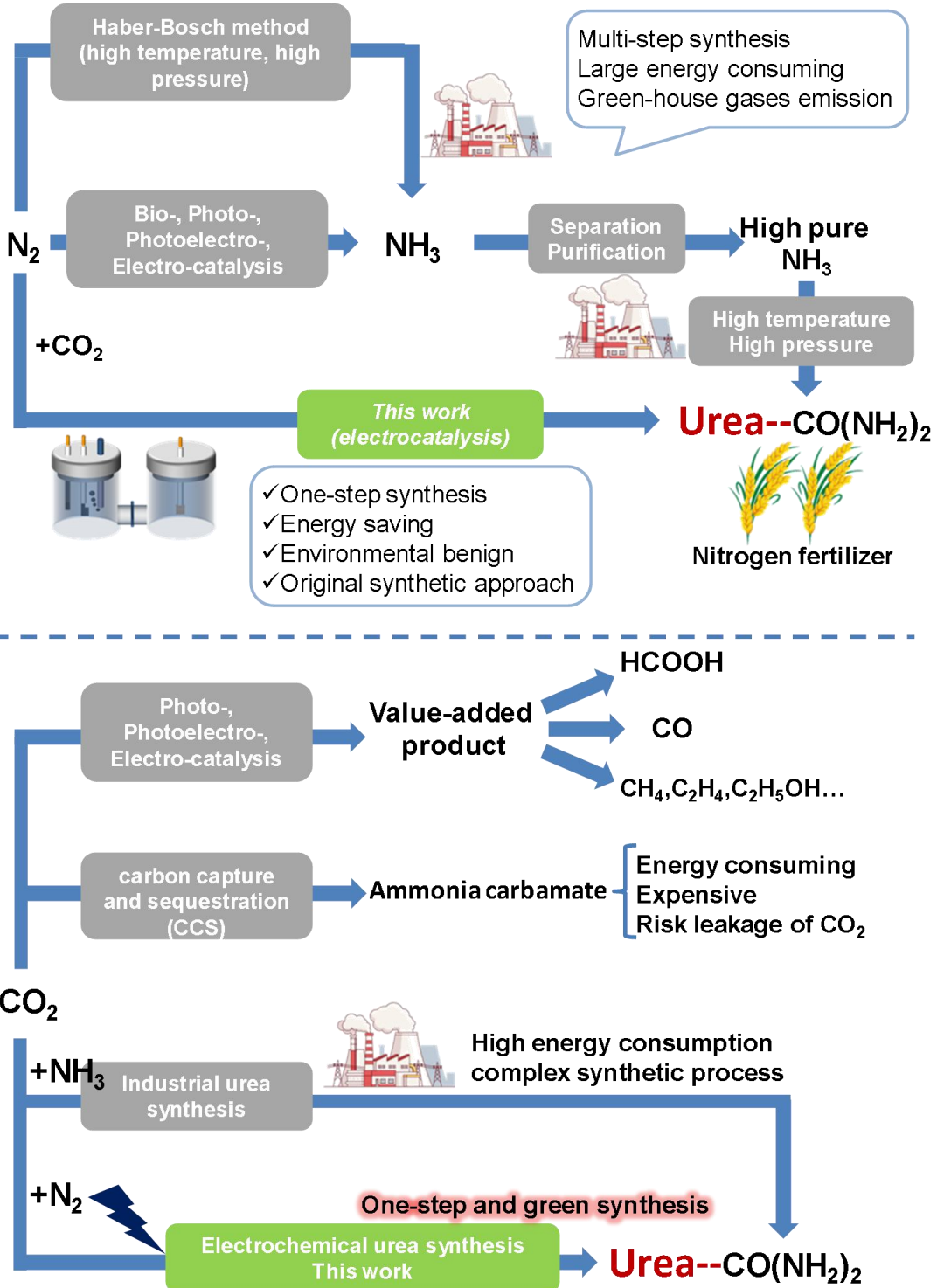
Supplementary Figure 30 | IR signals in the range 1100–1700 cm^{-1} under various potentials for pure glassy carbon during the electroreduction of CO_2 and N_2 processes.



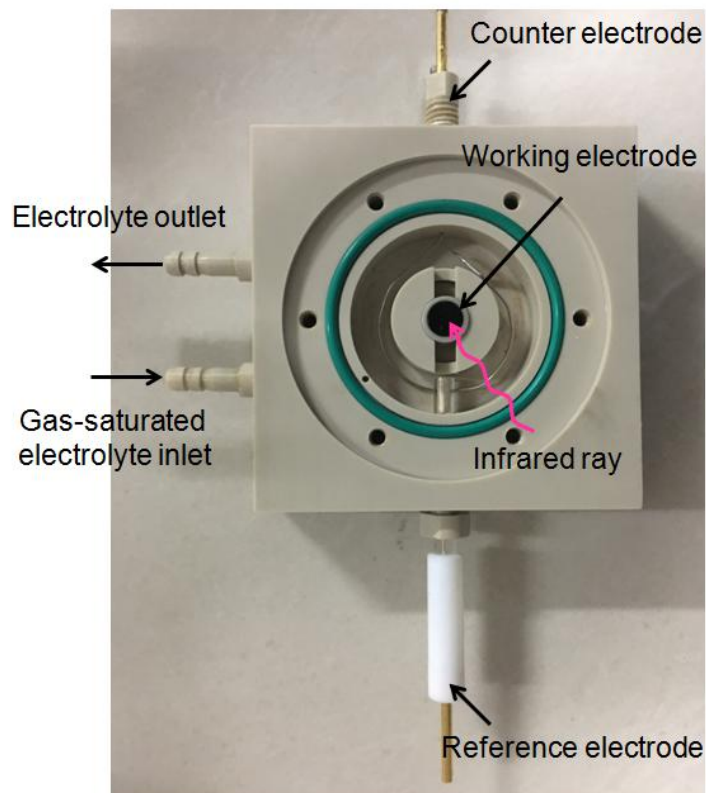
Supplementary Figure 31 | (a) Free energy diagram of the CO₂ reduction with and without the assist of N₂. Corresponding geometry structures with (b) and without (c) co-adsorbed N₂. The green, orange, blue, red, gray, and white balls represent Pd, Cu, N, O, C, and H atoms, respectively.



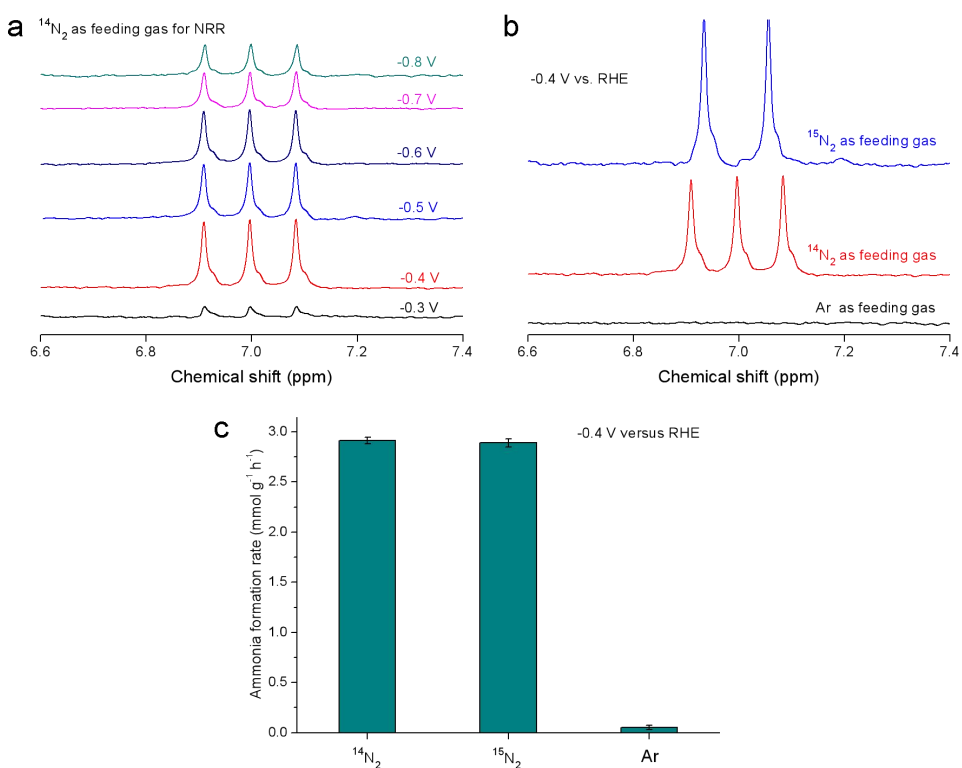
Supplementary Figure 32 | (a) A possible reaction mechanism of urea production. (b) The deformation charge density of Cu-Pd system. The green area indicates charge delocalization, while the red means charge localization. The isosurface was set to be $0.05 \text{ eV } \text{\AA}^{-1}$. (c) The electron localization function. The red part means electron localization while the blue part means the electron delocalization. (d) The free energy change along the minimum energy pathway of urea production at 0 V versus RHE and -0.4 V versus RHE.



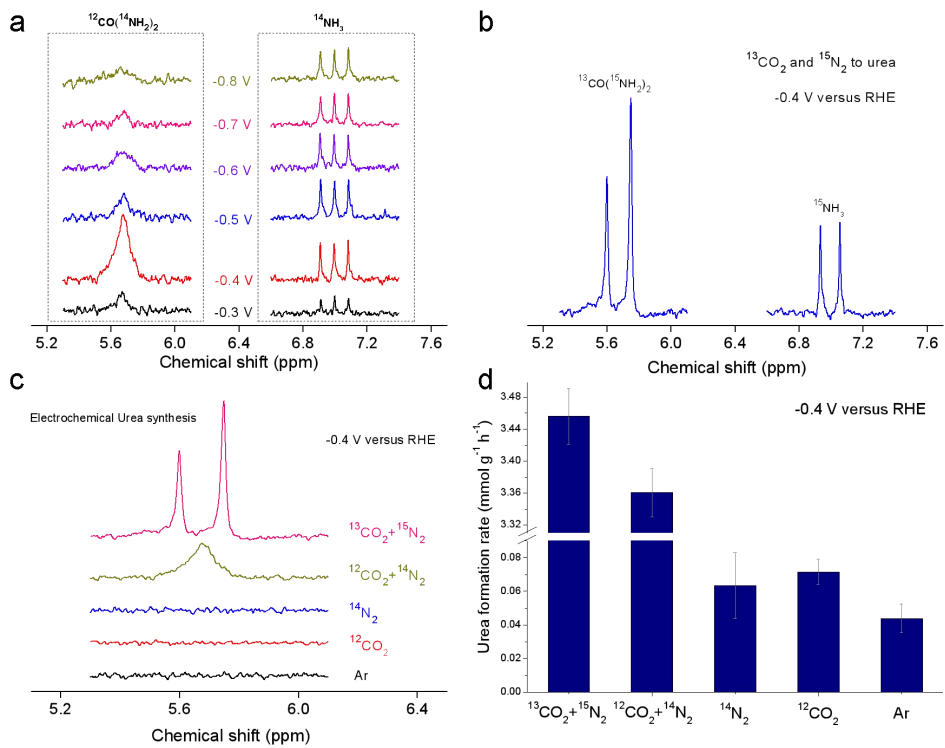
Supplementary Figure 33 | Schematic diagram for utilization of N_2 and CO_2 .



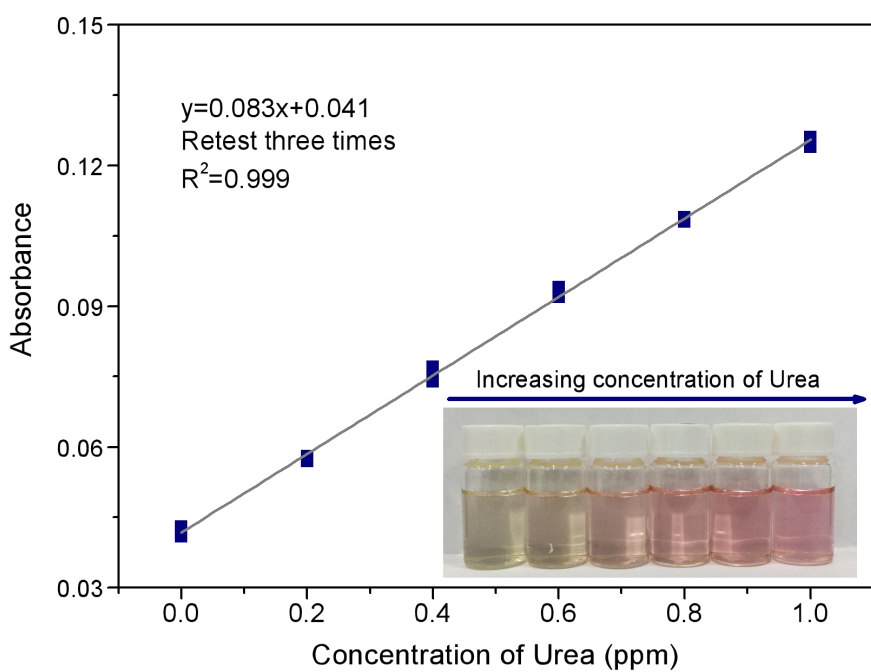
Supplementary Figure 34 | Schematic diagram of the electrochemical cell for *Operando* synchrotron radiation FTIR measurements.



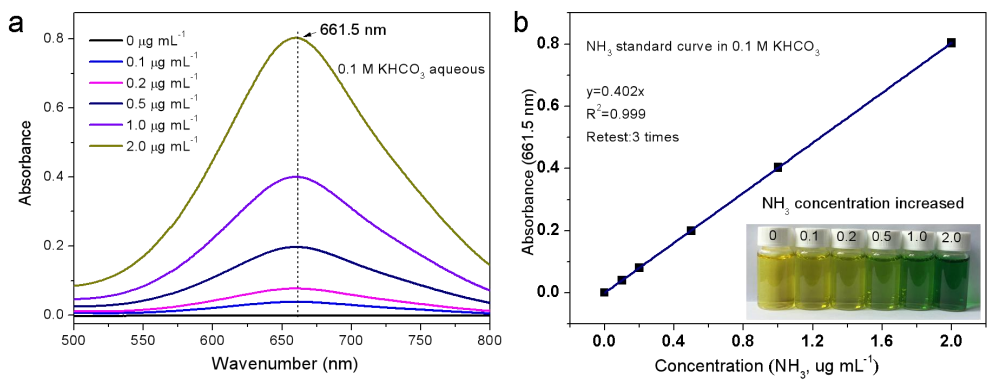
Supplementary Figure 35 | The identification and quantification for electrochemical ammonia synthesis. (a) The ^1H NMR spectra for ammonia synthesis under various applied potentials with $^{14}\text{N}_2$ as feeding gas. (b) The ^1H NMR spectra for ammonia synthesis at -0.4 V versus RHE with $^{14}\text{N}_2$, $^{15}\text{N}_2$ and Ar as feeding gas respectively. (c) The ammonia formation rates with $^{14}\text{N}_2$, $^{15}\text{N}_2$ and Ar as feeding gas respectively.



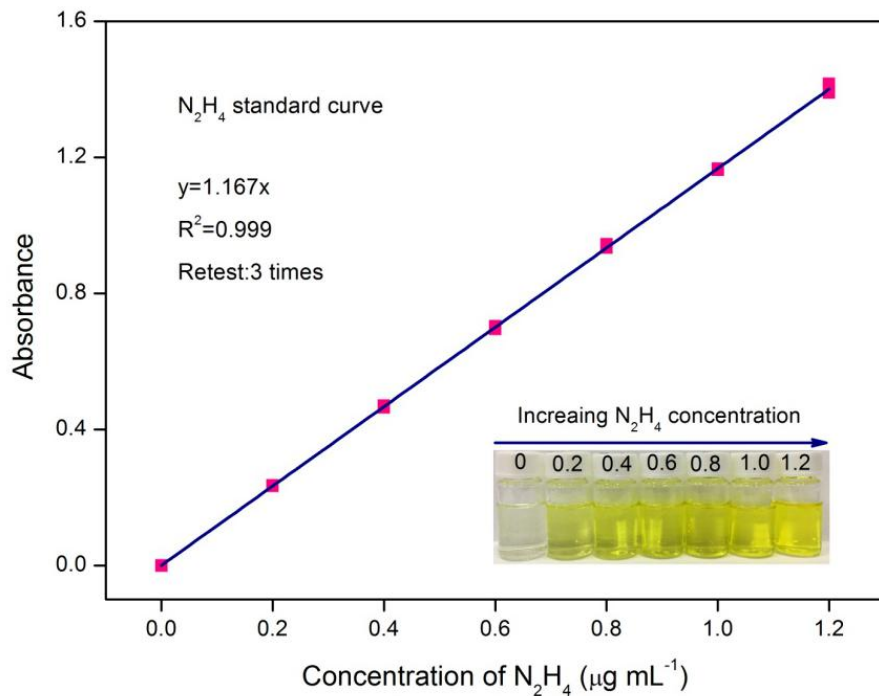
Supplementary Figure 36 | The identification and quantification for electrochemical urea synthesis. (a) The ¹H NMR spectra for urea synthesis under various applied potentials with ¹²CO₂ and ¹⁴N₂ as feeding gases. (b) The ¹H NMR spectra for urea synthesis with ¹³CO₂ and ¹⁵N₂ as feeding gases at -0.4 V versus RHE. (c) The ¹H NMR spectra for urea synthesis at -0.4 V versus RHE with ¹³CO₂ and ¹⁵N₂, ¹²CO₂ and ¹⁴N₂, ¹⁴N₂, ¹²CO₂ and Ar as feeding gases respectively. (d) The urea formation rates with ¹³CO₂ and ¹⁵N₂, ¹²CO₂ and ¹⁴N₂, ¹⁴N₂, ¹²CO₂ and Ar as feeding gases respectively.



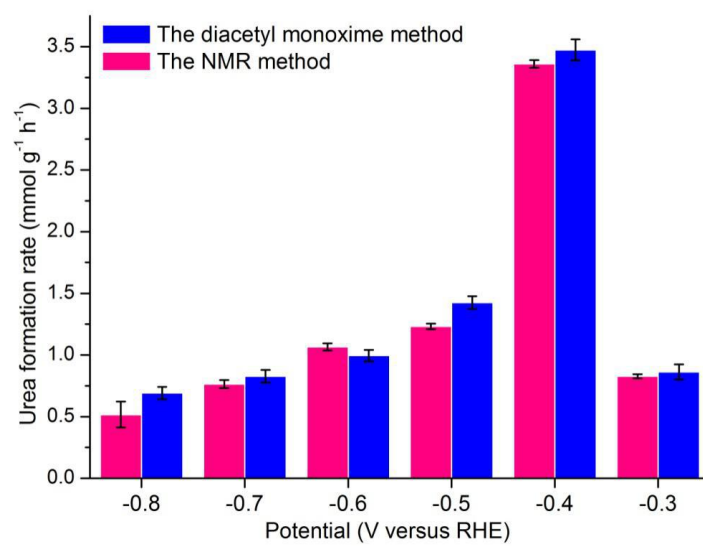
Supplementary Figure 37 | The quantification of urea concentration by diacetyl monoxime method². The color reagents are prepared as followed. *A*: acid-ferric solution. 100 ml concentrated phosphoric acid was mixed with 300 ml of concentrated sulfuric acid and 600 ml distilled water, then 100 mg ferric chloride was dissolved in the above solution. *B*: Diacetylmonoxime (DAMO)-thiosemicarbazide (TSC) solution. 5 g of DAMO and 100 mg TSC were dissolved in distilled water and diluted to 1000 ml. Subsequently, a series of urea standard solutions (0 ppm, 0.2 ppm, 0.4 ppm, 0.6 ppm, 0.8 ppm and 1 ppm) were prepared. For the color generation, 2 ml of *A* and 1 ml of *B* were added into 1 ml of urea-containing solution and mixed vigorously. Then, the solution was heated to 100 °C and maintained at this temperature for 15 min. After cooling to 25 °C, the absorbance was acquired at 525 nm. The calibration curve for quantification of urea indicates good linear relation of absorbance with urea concentration ($y=0.083x+0.041$, $R^2=0.999$) of three times independent calibration curves, the inset are the pictures of pink solutions with different urea concentrations.



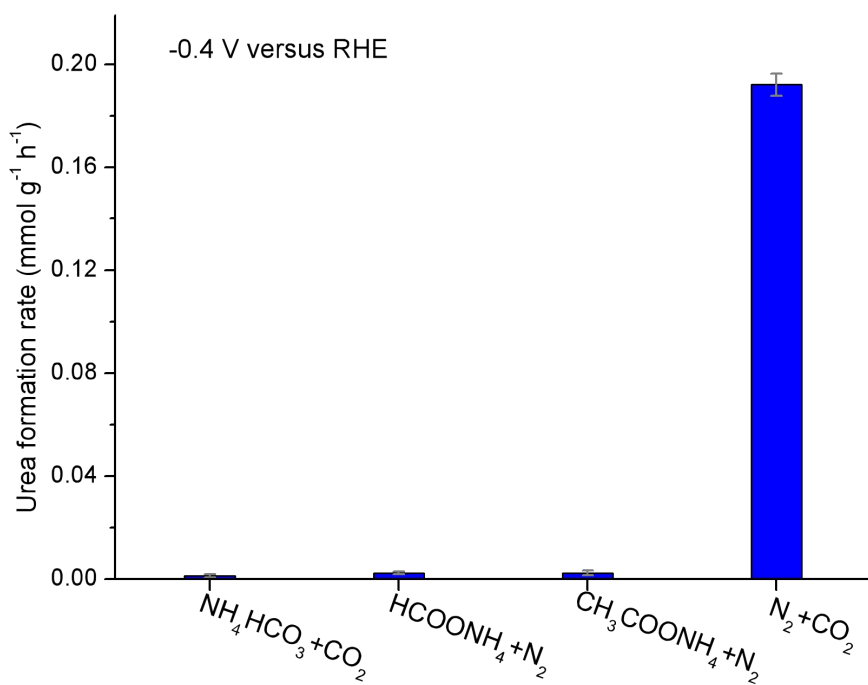
Supplementary Figure 38 | The quantification of ammonia concentration by the indophenols blue method³. (a) A series of standard solutions with ammonia concentrations of 0 ppm, 0.1 ppm, 0.2 ppm, 0.5 ppm, 1.0 ppm and 2.0 ppm respectively and the color regents (*A*: 1 M NaOH solution containing 5 wt% salicylic acid and 5 wt% sodium citrate; *B*: 0.05 M NaClO; *C*: 1 wt% sodium nitroferricyanide) were prepared firstly. Then, 2 mL of standard solution was transferred to a glass bottle and 2 mL of *A*, 1 mL of *B* and 0.2 mL of *C* were added in turn to the above bottle. The absorbance was measured in the range of 500 to 800 nm after the solution was reserved in dark for two hours. (b) Calibration curve used for quantification of ammonia concentration. The absorbance at 661.5 nm was measured by UV-Vis spectrophotometer, and the fitting curve shows good linear relation of absorbance with ammonia concentration ($y=0.402x$, $R^2=0.999$) of three times independent calibration curves.



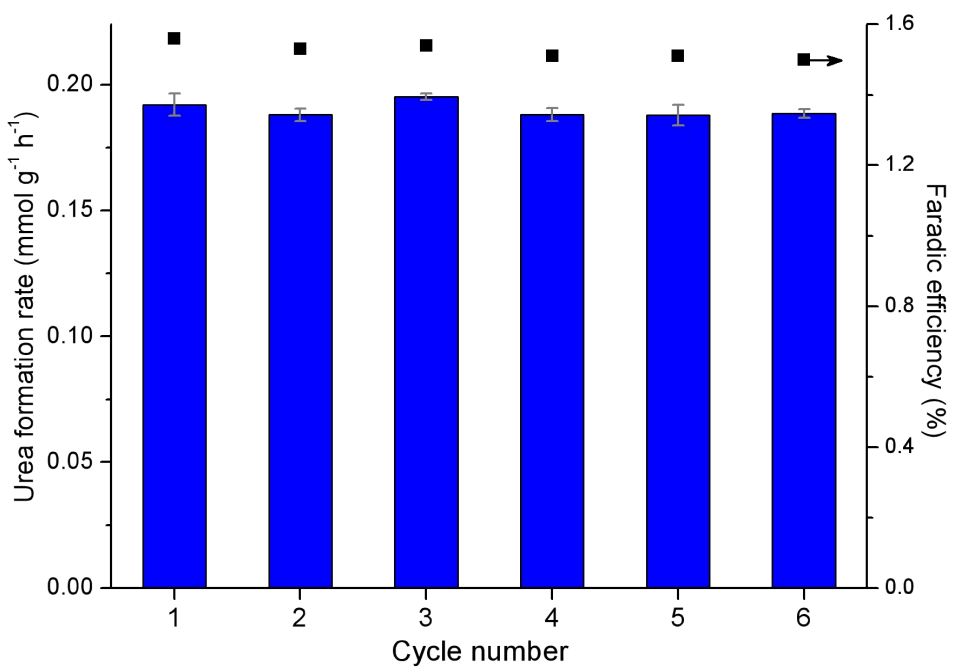
Supplementary Figure 39 | Calibration curve for colorimetric N₂H₄ assay in 0.1 M KHCO₃ by the method of Watt and Chrisp⁴. Series of standard solutions were prepared with the concentrations of 0, 0.2, 0.4, 0.6, 0.8, 1.0 and 1.2 μg mL⁻¹ (as N₂H₄) and absorbance at 458 nm were obtained after addition of color reagent for 20 min. The fitting curve shows good linear relation of absorbance with N₂H₄ concentration ($y=1.167x$, $R^2=0.999$) of three times independent calibration curves. The electrochemical characterization results indicate that barely any N₂H₄ was generated during the NRR tests or the electrochemical urea synthesis.



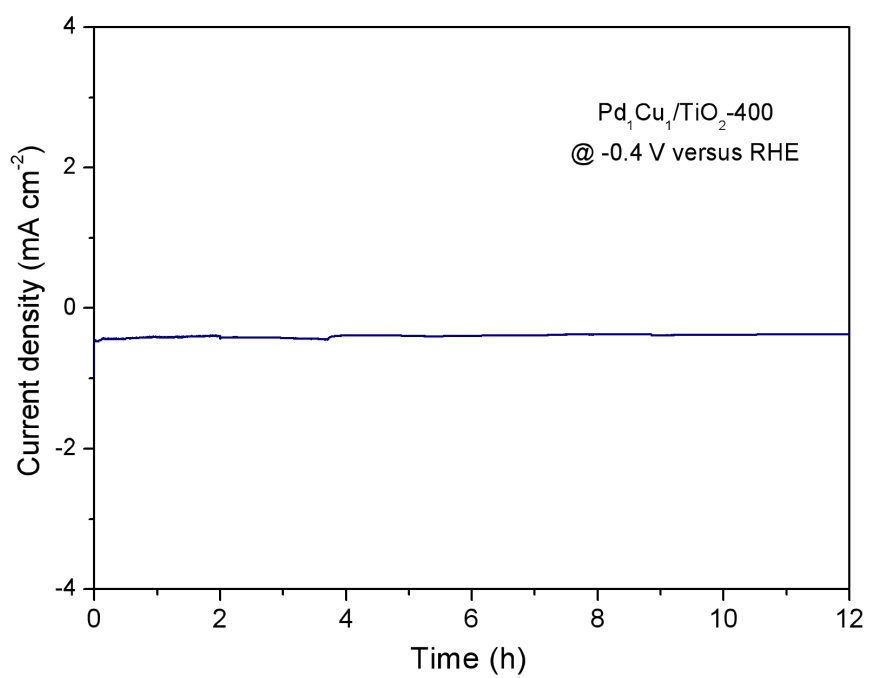
Supplementary Figure 40 | The urea formation rates quantified by the diacetyl monoxime method and the NMR spectroscopy.



Supplementary Figure 41 | The comparison of urea formation rate in H cell with N_2 and CO_2 as feeding stock and the urea synthesis in the presence of 100 ppm of NH_4HCO_3 with sole CO_2 as feeding gas, 100 ppm of HCOONH_4 with N_2 as feeding gas and 100 ppm of $\text{CH}_3\text{COONH}_4$ with N_2 as feeding gas respectively.



Supplementary Figure 42 | The stability test of Pd₁Cu₁/TiO₂-400 for 6 cycles at -0.4 V versus RHE in H cell.



Supplementary Figure 43 | Chronoamperometric curves of $\text{Pd}_1\text{Cu}_1/\text{TiO}_2\text{-400}$ at -0.4 V versus RHE for 12 h of electrocatalysis in H cell.

Supplementary Table 1 | Details for synthesis of electrocatalysts.

Sample	PdCl ₂ (ul, 5 mg ml ⁻¹)	CuCl ₂ ·2H ₂ O (ul, 5 mg ml ⁻¹)	TiO ₂	NaBH ₄
Pd/TiO ₂	255	0		
Pd ₃ Cu ₁ /TiO ₂	192	61		
Pd ₂ Cu ₁ /TiO ₂	170	82		
Pd ₁ Cu ₁ /TiO ₂	128	123	30 mg	50 mg
Pd ₁ Cu ₂ /TiO ₂	85	164		
Pd ₁ Cu ₃ /TiO ₂	64	184		
Cu/TiO ₂	0	246		

Supplementary Table 2 | Weight quantifications of Pd and Cu based on ICP-MS.

Sample	Pd (wt %)	Cu (wt %)	Molar ratio (Pd:Cu)	Practical structure
Pd ₁ Cu ₁ /TiO ₂	1.09	0.73	0.89:1	Pd _{0.89} Cu ₁ /TiO ₂
Pd ₁ Cu ₁ /TiO ₂ -200	1.02	0.72	0.85:1	Pd _{0.85} Cu ₁ /TiO ₂ -200
Pd ₁ Cu ₁ /TiO ₂ -400	1.13	0.77	0.88:1	Pd _{0.88} Cu ₁ /TiO ₂ -400
Pd ₁ Cu ₁ /TiO ₂ -600	1.07	0.72	0.89:1	Pd _{0.89} Cu ₁ /TiO ₂ -600
Pd/TiO ₂ -400	2.07	0		
Cu/TiO ₂ -400	0	1.48		

Supplementary Table 3 | Calculated zero point energies and entropy of different adsorption species, where the * denotes the adsorption site.

Species	E_{ZPE} (eV)	TS (eV)	$G-E_{elect}$ (eV)
N_2	0.15	-0.60	-0.45
CO_2	0.31	-0.66	-0.35
H_2	0.28	-0.42	-0.14
H_2O	0.56	-0.68	-0.12
* N_2	0.18	-0.13	+0.05
* $NCON^*$	0.39	-0.17	+0.22
* $NCONH$	0.71	-0.17	+0.54
* $NCONH_2$	1.05	-0.16	+0.89
* $NHCONH$	1.05	-0.20	+0.85
* $NHCONH_2$	1.41	-0.19	+1.22
* $COOH$	0.59	-0.21	+0.38
* CO	0.18	-0.14	+0.04

Supplementary References

1. Wang, J., Zhang, P., Li, X., Zhu, J. & Li, H. Synchronical pollutant degradation and H₂ production on a Ti³⁺-doped TiO₂ visible photocatalyst with dominant (001) facets. *Appl. Catal. B-Environ.* **134**, 198-204 (2013).
2. Rahmatullah, M. & Boyde, T. R. C. Improvements in the determination of urea using diacetyl monoxime; methods with and without deproteinisation. *Clin. Chim. Acta* **107**, 3-9 (1980).
3. Chen, C. et al. B-N Pairs Enriched Defective Carbon Nanosheets for Ammonia Synthesis with High Efficiency. *Small* 1805029 (2019).
4. Watt, G. W. & Chrisp, J. D. Spectrophotometric method for determination of hydrazine. *Anal. Chem.* **24**, 2006-2008 (1952).